Resolving the spatiotemporal distribution of substances in fluids using a deep learning method

Zhou, Zaiyang; Kuai, Yu; Huang, Kailin; van Maren, Dirk Sebastiaan; Pang, Jialin; Wang, Zhenwu; Zhu, Yonghui; Ge, Jianzhong

DOI
10.1080/19942060.2025.2564761

Publication date
2025

Document Version
Final published version

Published in
Engineering Applications of Computational Fluid Mechanics

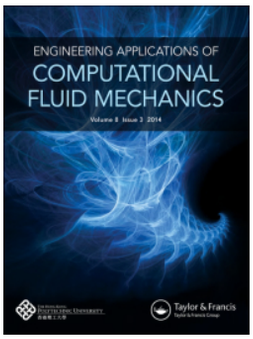

Engineering Applications of Computational Fluid Mechanics

ISSN: 1994-2060 (Print) 1997-003X (Online) Journal homepage: www.tandfonline.com/journals/tcfm20

Resolving the spatiotemporal distribution of substances in fluids using a deep learning method

Zaiyang Zhou , Yu Kuai , Kailin Huang , Dirk Sebastiaan van Maren , Jialin Pang , Zhenwu Wang , Yonghui Zhu & Jianzhong Ge

To cite this article: Zaiyang Zhou , Yu Kuai , Kailin Huang , Dirk Sebastiaan van Maren , Jialin Pang , Zhenwu Wang , Yonghui Zhu & Jianzhong Ge (2025) Resolving the spatiotemporal distribution of substances in fluids using a deep learning method, Engineering Applications of Computational Fluid Mechanics, 19:1, 2564761, DOI: 10.1080/19942060.2025.2564761

To link to this article: https://doi.org/10.1080/19942060.2025.2564761

ENGINEERING APPLICATIONS OF COMPUTATIONAL FLUID MECHANICS
2025, VOL. 19, NO. 1, 2564761
https://doi.org/10.1080/19942060.2025.2564761

Resolving the spatiotemporal distribution of substances in fluids using a deep learning method

Zaiyang Zhou[a], Yu Kuai[b], Kailin Huang[c], Dirk Sebastiaan van Maren[b,d], Jialin Pang[a], Zhenwu Wang[a], Yonghui Zhu[e] and Jianzhong Ge[a]

[a]State Key Laboratory of Estuarine and Coastal Research, East China Normal University, Shanghai, People's Republic of China; [b]Faculty of Civil Engineering and Geosciences, Delft University of Technology, Delft, The Netherlands; [c]State Key Laboratory of Water Resources Engineering and Management, Wuhan University, Wuhan, People's Republic of China; [d]Unit of Marine and Coastal Systems, Deltares, Delft, The Netherlands; [e]Changjiang River Scientific Research Institute, Changjiang Water Resources Commission, Wuhan, People's Republic of China

ABSTRACT

Accurate and efficient prediction of spatiotemporal variations in the distribution of substances in fluids (SIFs) is crucial for various aspects of fluid mechanics related research and applications, involving for instance, material transport quantification, water quality assessment, and engineering condition analysis. This study proposes a framework for resolving the spatiotemporal distribution of SIFs such as salt and suspended sediment based on water levels and flow velocities. The framework incorporates a deep learning model based on a classic neural operator (DeepONet) architecture, which consists of a feature network and a position network to encode the characteristics of input variables and the problem domain. Numerical simulations were performed to generate the needed datasets. The framework was well-validated by predicting salinity and suspended sediment concentration (SSC) distributions in two idealized cases and a real-word case, demonstrating its efficacy and robustness. Time-series validation further demonstrated the prediction accuracy of the framework. The deep learning model is also capable of enhanced-resolution predictions, enabling the generation of high-resolution spatial distributions of SIFs from low-resolution hydrodynamic data. Both bottom and surface layers of the water column were analyzed, revealing that the mapping relationships between hydrodynamics and SIF distributions can be accurately captured throughout the water column, despite variations in correlation coefficients. Due to these capabilities and advantages, additional data sources can be integrated into the framework in the future, highlighting its considerable potential for broader applications in aquatic environments.

ARTICLE HISTORY
Received 28 March 2025
Accepted 8 September 2025

KEYWORDS
Spatiotemporal prediction; salinity; suspended sediment concentration; deep learning; enhanced resolution

1. Introduction

1.1. Motivation

The transport and distribution of Substances in Fluids (SIFs), driven by fluid motions, significantly influence human activities and marine ecosystems. For instance, nutrient transport may lead to eutrophication and hypoxia (Stoecker et al., 2017). Consequently, numerous studies have extensively investigated the transport mechanisms and source-sink dynamics of SIFs (Amoudry & Souza, 2011; Huettel et al., 2014; Xie et al., 2024). Among various substances, salt and suspended sediment are fundamental and can significantly influence water systems. Salt transport is closely associated with saltwater intrusion, a significant threat to freshwater resources (Ge et al., 2022; Wu et al., 2010) that severely jeopardizes water security and profoundly impacts ecology, biogeochemistry, and the economy (Luo et al., 2023; Mondal et al., 2023). In contrast to salt, which exists in ionic dissolved form in water, sediment exists in granular particle form. In addition to its direct influence on shaping topography, thereby affecting channel navigability (Garcia et al., 2024) and structural safety (Zhang et al., 2024), sediment interacts in complex ways with other SIFs. For example, the adsorption capacity of sediment can regulate the behavior of heavy metals in aquatic environments (Miranda et al., 2021). It also modulates the dynamics of nutrients and phytoplankton (Ge et al., 2020). Given these factors, predicting the spatiotemporal distribution of salt and suspended sediment is of considerable scientific and practical value and serves as an ideal starting point for predicting other SIFs.

CONTACT Jianzhong Ge jzge@sklec.ecnu.edu.cn State Key Laboratory of Estuarine and Coastal Research, East China Normal University, Shanghai, 200241, People's Republic of China

Supplemental data for this article can be accessed online at https://doi.org/10.1080/19942060.2025.2564761.

A prevalent conventional approach for investigating the spatiotemporal variations in SIFs is the use of process-based numerical models (e.g. Cugier & Le Hir, 2002; Lesser et al., 2004; Papanicolaou et al., 2008; Zhou et al., 2025). These models have significantly advanced our understanding of detailed mechanisms, yet they are still limited by the incomplete incorporation of all underlying processes (Hunter et al., 2018). This is especially the case for fine sediment dynamics: numerically modeling all processes driving fine sediment transport requires a level of processes knowledge, model input, and resolution which cannot be resolved by the current generation of models and requires user-defined simplifications of actual processes (Winterwerp et al., 2021). Additionally, the computational efficiency of numerical models may become a limiting factor when short computational periods are of paramount importance, for instance, in disaster forecasting. Both the complexity of accurately predicting SIFs (especially sediments) and the associated computational time motivate the exploration of alternatives to numerical models for predicting their spatiotemporal evolution. Data-driven models could provide such an alternative, initially trained by SIFs computed by numerical models but in the future possibly relying on other data sources such as satellite-derived data. We therefore explore the capacity of existing deep learning techniques to advance our predictive capabilities of SIFs, focusing on salinity and sediments.

1.2. Related works

Recently, substantial efforts have been devoted to developing data-driven models for predicting the transport and distribution of SIFs using state-of-the-art machine learning (ML) techniques (Feizizadeh et al., 2021; Goldstein et al., 2019). For example, time-series variations in salinity and suspended sediment concentration (SSC) at individual sites can be forecasted based on the target variable itself (Zhang et al., 2022) or several other variables (Wang & Ge, 2025). However, to the best of the authors' knowledge, ML-based spatiotemporal predictions of SIFs are both rare and challenging, even though understanding the spatiotemporal variations of these variables is essential for comprehending their evolutionary patterns and potential impacts. In fact, the cutting-edge deep learning (DL) architectures and their numerous variants have been extensively studied and applied for spatiotemporal predictions, more frequently in meteorology compared to water research. Such DL models for weather forecasting include FourCastNet (Pathak et al., 2022), Pangu-Weather (Bi et al., 2023), GraphCast (Lam et al., 2023), etc. These models often link predicted variables with dozens of other variables and achieve superior inference efficiency, thereby they need substantial and well-structured data for training and inference.

However, meeting these data requirements remains a significant challenge for various water systems, such as large rivers, estuaries, and oceans. For these environments, it is difficult to acquire datasets that encompass multiple variables, cover extensive spatial ranges, and maintain relatively consistent resolution, especially for the lower layers of the water column, which are beyond the reach of satellite imagery. This situation limits the data-driven spatial prediction, leading most previous research to focus on predictions for scattered sites (e.g. Song et al., 2020). Although other DL models such as physics-informed neural networks (PINN) can alleviate the data dependency and resolve multiple variables like water levels and current velocities by fitting the governing equations (Zhou et al., 2025b), difficulties in incorporating complex real-world boundary conditions and training the model limit their applications in real-time prediction. Therefore, constructing a data-driven DL model based on potentially available data is crucial for predicting the spatiotemporal distribution of SIFs.

1.3. Hypothesis and contribution

In most cases, fundamental hydrodynamic variables such as water levels and current velocities are the most readily available data. For example, global navigation satellite system (GNSS) can provide accurate large-scale water levels (Wang et al., 2021), satellite-based velocity products are also available in coastal environments (Martin et al., 2022), and image-based hydrometry techniques can effectively monitor flow conditions (Eltner et al., 2018; Gilmore et al., 2013; Huang et al., 2024). Even when such data are unavailable, numerical simulations of pure hydrodynamics are much faster than simulations including various SIFs. Therefore, it is crucial to examine whether significant mapping relationships exist between basic hydrodynamics and SIFs and to what extent these relationships can be captured by data-driven models instead of partial differential equation (PDE) solvers. If confirmed, these mapping relationships could be leveraged to infer the distribution of SIFs directly from hydrodynamic information. In this study, we establish such a framework that uses water levels and current velocities as inputs to predict the distribution of salinity and SSC using a DL model. Critically, we prove the ability of this DL model to enhance prediction resolution, by examining whether it can predict the high-resolution substance distributions with low-resolution hydrodynamic inputs. This enhanced-resolution capability demonstrates greater potential in overcoming the limitation of data scarcity.

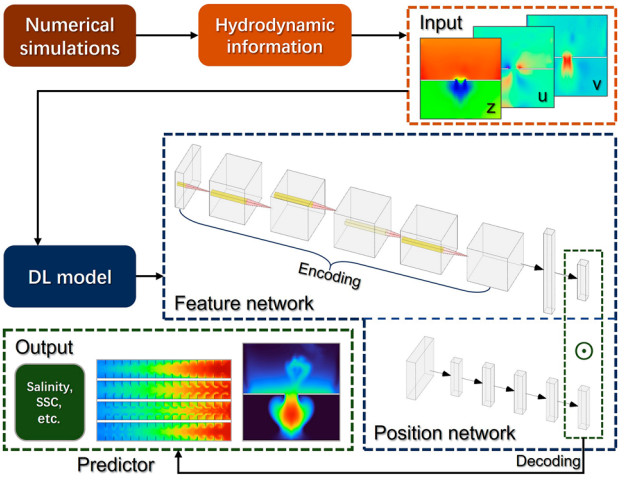

Figure 1. A schematic visualization of the framework; *z*, *u*, and *v* denote water level, eastward velocity component, and northward velocity component, respectively. The symbol '⊙' signifies Hadamard product.

2. Methods

The framework proposed in this study can be summarized in three main steps, (1) Data Generation: using numerical models to provide hydrodynamic information on water levels and current velocities, as well as the corresponding distribution of substances; (2) DL Model Training: training the model to capture the mapping relationship between hydrodynamics and substance distribution; (3) Prediction: using the well-trained DL model to infer substance distribution based on fundamental hydrodynamics, i.e. water levels and flow velocities. A schematic visualization of this framework is presented in Figure 1. Detailed descriptions of the DL model, numerical cases, and data preparation are provided in the following subsections.

2.1. Deep learning model

The DL model is constructed based on a deep operator network (DeepONet). Inspired by the universal approximation theorem for nonlinear operators (Chen and Chen, 1995), DeepONet is a notable neural network architecture capable of learning the nonlinear operator that maps from one function space to another (Lu et al., 2021). For example, it can learn implicit operators like integration, fractional derivative (1D), and fractional Laplacians (2D), indicating that this architecture can be used for stochastic and parametric PDEs. Recently, advanced DeepONet-based models have been developed and applied in a variety of fields. For instance, S-DeepONet incorporates sequential learning models to capture causal relationships in time-dependent input data (He et al., 2024). Due to its capability for operator regression between function spaces, a DeepONet-based model is designed and optimized to approximate mappings between basic hydrodynamics and substance distribution.

The DeepONet architecture consists of two types of sub-networks, namely the branch networks and the trunk networks. The branch network encodes input source functions, and the trunk net encodes the domain geometry. Specifically, in our model, the branch network processes the discretized representation of the input functions, i.e. 2-D structured water levels and velocity components at multiple time stamps. The trunk net typically takes position information as input, e.g. spatial coordinates (x, y). Therefore, in our framework they are referred to as the feature network and position network, respectively, for greater clarity. The final output of the DL model is obtained by the element-wise multiplication of both networks as in,

$$\begin{aligned} S^{\theta}(x,y) &= G(z,u,v)(x,y) \\ &= \sum_{k=1}^{M} f_k(z,u,v) \odot p_k(x,y) \end{aligned} \tag{1}$$

where x, y are positional coordinates; z, u, v represent water levels, eastward component, and northward component of current velocities; θ means trainable parameters of the neural network; $S^{\theta}(x,y)$ is the predicted substance distribution at (x,y) given parameters θ; $G: (z,u,v) \rightarrow S^{\theta}$ is a nonlinear operator that represents the mapping relationship between hydrodynamics and substance distribution; f_k and p_k represent outputs of feature network and position network; M means the number of outputs of both feature and position networks; $\odot$ means Hadamard product. With the Hadamard product of feature and position networks, nonlinear interaction between latent vectors of these two sub-networks can be expressed (Li & Shatarah, 2024).

The original DeepONet employs feed-forward neural networks (FNNs), implemented by multi-layer perceptron (MLP), for both the branch and trunk networks. To better extract spatiotemporal information from hydrodynamic inputs and enable resolution-enhanced inference capabilities (P. Wang et al., 2022), convolutional neural networks (CNNs), which have been widely used in 2-D data processing (Mei et al., 2024), are applied to encode multiple input variables. The feature network includes 4 convolutional layers, along with additional average pooling and dropout layers to control overfitting and enhance the generalization capability of the model. The position network takes the (x, y) coordinates as input to encode the problem domain, using 3 fully connected layers. These coordinates are organized in the same 2-D dimension as the input features for consistency. The

Table 1. List of main layers in the DL model.

No.	Layer	Output size	Layer property	Size-in	Size-out
Feature network					
1	Conv2D	96	2×2	$[H, W, 3]$	$[(H-1), (W-1), 96]$
2	Conv2D	128	3 × 3	$[(H-1), (W-1), 96]$	$[(H-3), (W-3), 128]$
3	Conv2D	192	3 × 3	$[(H-3), (W-3), 128]$	$[(H-5), (W-5), 192]$
4	Conv2D	192	3 × 3	$[(H-5), (W-5), 192]$	$[(H-7), (W-7), 192]$
5	AvgPool2D	192	3 × 3	$[(H-7), (W-7), 192]$	$[(H-9), (W-9), 192]$
6	Flatten	/	/	$[(H-9), (W-9), 192]$	$[(H-9) \times (W-9) \times 192, 1]$
7	FC	1280	/	$[(H-9) \times (W-9) \times 192, 1]$	[1280, 1]
8	Dropout	/	0.1	[1280, 1]	[1280, 1]
9	FC_F	1280	/	[1280, 1]	[1280, 1]
Position network					
1	FC	1280	/	$[H, W, 2]$	[1280, 1]
2	FC	1280	/	[1280, 1]	[1280, 1]
3	FC	1280	/	[1280, 1]	[1280, 1]
4	Dropout	/	0.1	[1280, 1]	[1280, 1]
5	FC_P	1280	/	[1280, 1]	[1280, 1]
Combination of feature and position networks					
1	Element-wise Multiplication	/	/	[1280, 1]	[1280, 1]
2	FC_out	$H \times W$	/	[1280, 1]	$[H \times W, 1]$

[*H*, *W*] indicates the height and width of the input matrix for both feature and position networks; while for their input dimensions, '3' corresponding to the number of applied features (i.e. *z*, *u*, *v*), and '2' corresponding to 2D positional dimensions (i.e. *x*, *y*). 'Conv2D', a 2D convolutional layer; 'AvgPool2D', a 2D average pooling layer; 'FC', a fully-connected layer; 'FC_F', 'FC_P', 'FC_out' represent the output FC layers of the feature network, the position network, and the whole DL model, respectively. Layer property indicates kernel size for CNN layers and dropout probability for dropout layers. The activation layers (ReLU) between main layers are omitted.

outputs of the feature and position networks are then multiplied elementwise and passed through a fully connected layer to produce an $H \times W$ matrix representing the substance distribution. Detailed information about the entire architecture is provided in Table 1.

The loss function is defined as,

$$\mathcal{L}(\theta) = MSE(S(x, y), S^{\theta}(x, y)) \tag{2}$$

where S denotes the ground-truth data, i.e. the numerical modeling results in this study, *MSE* signifies the mean squared error calculation (L2 loss). The trainable parameters θ are thereby optimized by minimizing $\mathcal{L}(\theta)$,

$$\theta^* = \arg\min_{\theta} \mathcal{L}_{\theta} \tag{3}$$

The method of stochastic gradient descent with momentum (SGDM) is applied to train the model with a constant learning rate of 0.02. The DL model is developed using MATLAB® R2024b and implemented on an NVIDIA RTX 4090 GPU with an Intel Core i9-14900 K processor. For the standard scenarios, it takes approximately 3.2 hours to train for 50,000 epochs.

The ground truth data (including hydrodynamics and target substance distribution) for the DL model in this study are derived from numerical simulations. It is important to note that while numerical models are used here, they are not essential for the DL model's functionality. Other data sources, such as re-analysis datasets or satellite images, can provide the necessary data in real-world applications; however, for aquatic environments, especially the lower layers of the water column, their availability is limited (as explained above). Numerical simulations enable us to investigate and compare the bottom and surface layers and easily control the spatial resolution for conducting enhanced-resolution tests. In the following sections, we introduce two idealized numerical models that focus on simulations of salinity and SSC, respectively.

2.2. Numerical models

Two idealized cases and one realistic case are set up using the Finite-Volume Coastal Ocean Model (FVCOM), a 3D primitive equation coastal ocean model operating on unstructured triangular grids. The unstructured grid allows the model to accurately fit the complex boundaries of coastlines and adopt flexible horizontal resolution. FVCOM has been widely employed to address scientific and practical problems related to hydrodynamics, sediment dynamics, biogeochemistry in both complex geometries (Beardsley et al., 2013; Guo et al., 2018; Shi et al., 2022) and simplified environments (Chen et al., 2009; Wu et al., 2011). Overall validation for the numerical scheme and model accuracy can be found in Chen et al. (2007). In particular, the FVCOM model has been extensively used to model salinity (Ge et al., 2022; Xue et al., 2009) and SSC (Morales-Marin et al., 2018; Zhou et al., 2021) distributions, demonstrating its effectiveness as a tool for generating datasets for the DL model. In this section, two idealized cases are introduced in detail, and the primary results based on these cases are presented in Sections 3.1–3.5. The results from a realistic case of

the North Passage of the Changjiang Estuary are presented separately in Section 3.6 to discuss the engineering applicability of the proposed approach.

2.2.1. The engineered channel case

In the first case, hydrodynamics and salt transport in an engineered channel of an estuarine system are simulated (Figure 2). This idealized model was established to investigate the effects of dikes and groynes on hydrodynamics and saltwater intrusion (Zhou et al., 2024). The schematization and spatial scale of the geometry are based on the North Passage, the main navigational channel of the Changjiang Estuary (Figure 2a). Along the open sea boundary ($x = 420$ km), tidal amplitudes and phases of 8 major astronomical tidal constituents (M_2, S_2, N_2, K_2, K_1, O_1, P_1, Q_1) are specified to resolve neap and spring tidal variations in hydrodynamics. At the upstream river boundary ($x = 0$ km), a constant river discharge of 3,000 m^3/s is prescribed. Detailed configuration and validation for this model can be found in Zhou et al. (2024). The channel system ($300 < x < 390$ km, $-5 < y < 5$ km) shown in Figure 2b is the focus of this study, with a grid resolution of 200 m.

This engineered channel case provides a dataset containing spatiotemporal variations in water levels (Figure 2c) and current velocities (Figure 2d and e) as input data, along with the salinity field as output data for the target region, at a temporal resolution of 10 minutes following a spin-up time of 10 days. A detailed description of the dataset will be provided in Section 2.1.3.

2.2.2. The tidal inlet case

A tidal inlet case is incorporated to provide a suspended sediment dataset for the DL model. Tidal inlet systems are found in many parts of the world (Ridderinkhof et al., 2014), typically consisting of coasts, back-barrier basins, barrier islands, and open sea areas with ebb tidal deltas (de Swart & Zimmerman, 2009).

We use a schematized tidal inlet numerical case inspired by the FVCOM model developed by Wu et al. (2011) (Figure 3a). The grid resolution is uniformly set to 200 m within the 15.2 km × 14.0 km model domain. Two 6.6 km × 0.2 km symmetric barrier islands are deployed, leaving an inlet width of 2.0 km. On the open sea boundary ($y = 14$ km), the same tidal information is used as in the engineered channel case. To comprehensively test the performance of the DL model, the effects of waves (Figure 3b) and winds are considered to generate an asymmetric and more complex distribution of suspended sediment. Wave conditions are calculated using the SWAN model. An additional constant southwesterly wind of 4.24 m/s (consisting of southerly and westerly components of 3 m/s each) is applied to the surface in the FVCOM model. Similar to the engineered channel case, a spin-up time of 10 days is adopted, but the output interval of this model is extended to 1 hour to cover more spring-neap cycles.

Since bathymetry is a dominant variable with a significant impact on hydrodynamics and sediment dynamics (Olabarrieta et al., 2014), the model calculates morphological evolutions. The inlet demonstrates a deepened pattern (Figure 3c) compared to the initial bathymetry (Figure 3a). Although the morphological evolution presented here does not show funnel-shaped extension in the back-barrier basin reported in previous studies, the deepened tidal channel aligns with findings in the literature (e.g. Bosboom & Reniers, 2014; Roelvink, 2006). This discrepancy could be due to the morphologically short simulation period. However, the primary aim of this numerical case is to provide a suspended sediment dataset with periodical variations superimposed on nonlinear trends rather than to validate a morphodynamic model. In summary, water levels and current velocity components in the x, y directions (Figure 3d–f) are provided by this simulation for the DL model to predict the SSC.

2.3. Data preparation and scenarios of the DL model

The salinity dataset contains 1,000 samples at a temporal resolution of 10 minutes (covering 7 days approximately), and the SSC dataset contains 1,440 samples with an interval of 1 hour (spanning 60 days in total). For main scenarios, a 75%-5%-20% split is applied to divide the datasets into training, validation, and test sets except for Case T-1∗ which applies a 60%-5%-35% split to evaluate the impact of reduced training data. The reduction of training data (from 75% to 60%) does not significantly affect model performance and detailed results can be found in the supplementary material. Table 2 summarizes the different scenarios that will be analyzed in detail. The standard scenarios (E-1 and T-1) employ a reproducible random sampling approach with the same random seed (an initializer for generating pseudorandom number). Additionally, two alternative partitioning strategies of the training, validation, and testing data are evaluated. The first scenario (T-2) partitions the datasets in chronological order according to the 75%-5%-20% split (Figure 4). This scenario tests whether the DL model can continuously capture and reconstruct a spring-neap tidal period by learning from three previous spring-neap cycles (75% of 60 days). Moreover, it is found that the SSC data exhibit a non-uniform distribution during the recording period with an overarching downward trend; the chronological order thus results in a larger range and average of SSC in

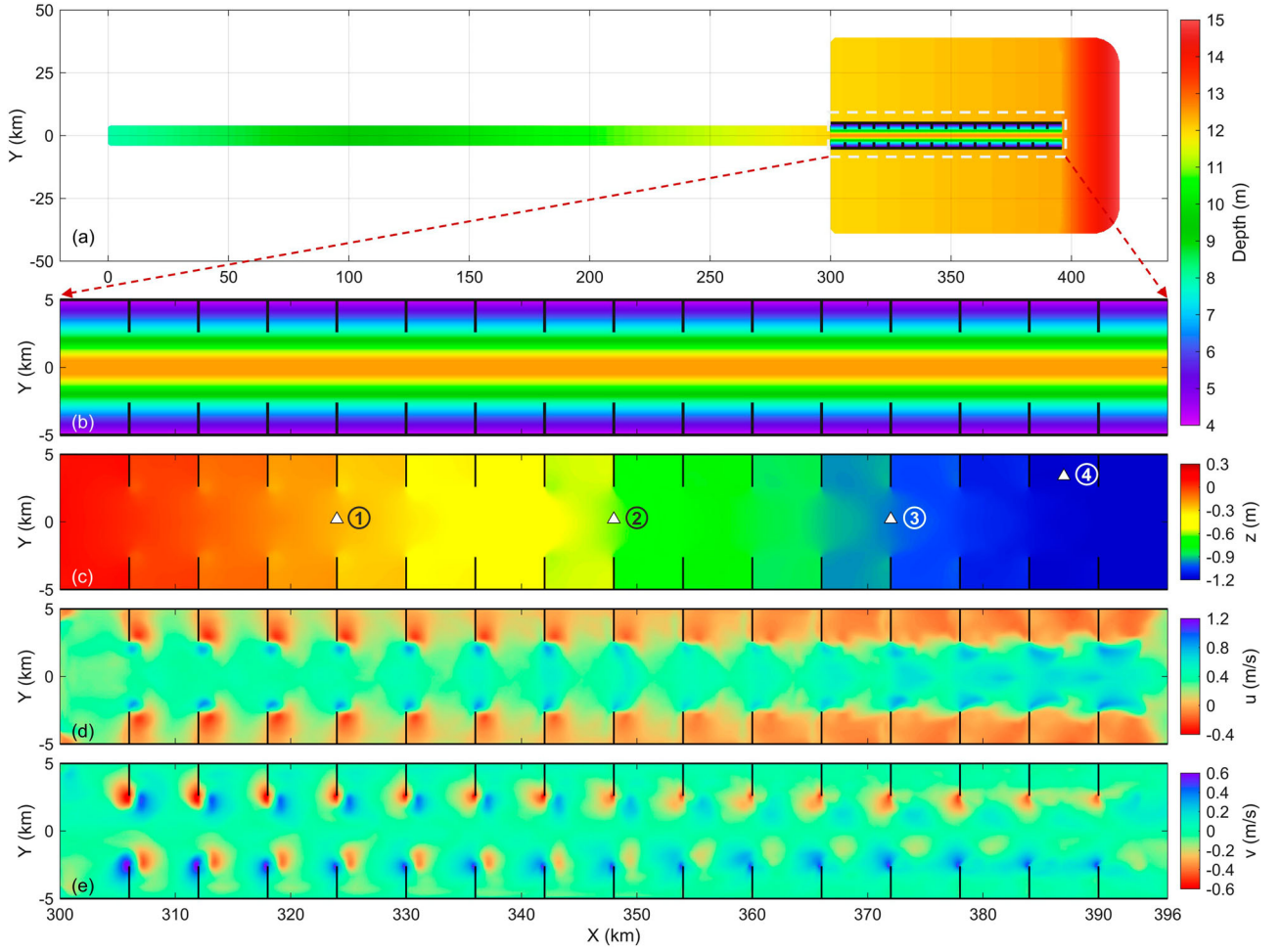

Figure 2. (a) Domain and bathymetry of the idealized model; (b) zoomed-in view of the main channel with the construction of dikes and groynes. Black lines indicate the engineering structures of dikes and groynes. An example snapshot of the dataset is presented, including the (c) water level, (d) eastward, and (e) northward components of current velocity in the bottom layer. White triangles in panel (c) represent four sites selected for time-series validation.

Table 2. A summary of all scenarios of the DL model, excluding Case T-4, which involves direct interpolation between data of different horizontal resolutions.

	Input resolution	Output resolution	Input variables	Output variables	Note
The engineered channel case					
E-1	(1000 m, 400 m)	(1000 m, 400 m)	z, u, v	Salinity	Random partitioning
The tidal inlet case					
T-1	(400 m, 400 m)	(400 m, 400 m)	z, u, v	SSC	Random partitioning
T-1∗	(400 m, 400 m)	(400 m, 400 m)	z, u, v	SSC	Training set reduced to 60%
T-2	(400 m, 400 m)	(400 m, 400 m)	z, u, v	SSC	Chronological partitioning
T-3	(400 m, 400 m)	(400 m, 400 m)	z, u, v	SSC	Inverse-order partitioning
T-4	(800 m, 800 m)	(200 m, 200 m)	SSC	SSC	Interpolation
T-5	(800 m, 800 m)	(200 m, 200 m)	z, u, v	SSC	Enhanced resolution
T-6	(400 m, 400 m)	(400 m, 400 m)	z, u, v	SSC	Surface layer
The North Passage case					
N-1	(0.005°, 0.005°)	(0.005°, 0.005°)	z, u, v	Salinity	Random partitioning

the training set. To test the model's capability to predict SSC increase, an inverse order data sampling (Figure 4) scenario (T3) is executed as well.

The spatial resolutions of both numerical cases are set to 200 m, corresponding to the highest resolution of the salinity and SSC datasets. However, a relatively lower resolution is adopted for standard scenarios to improve training efficiency and facilitate a more comprehensive discussion of the model performance in enhanced-resolution prediction. In the standard scenarios, the input

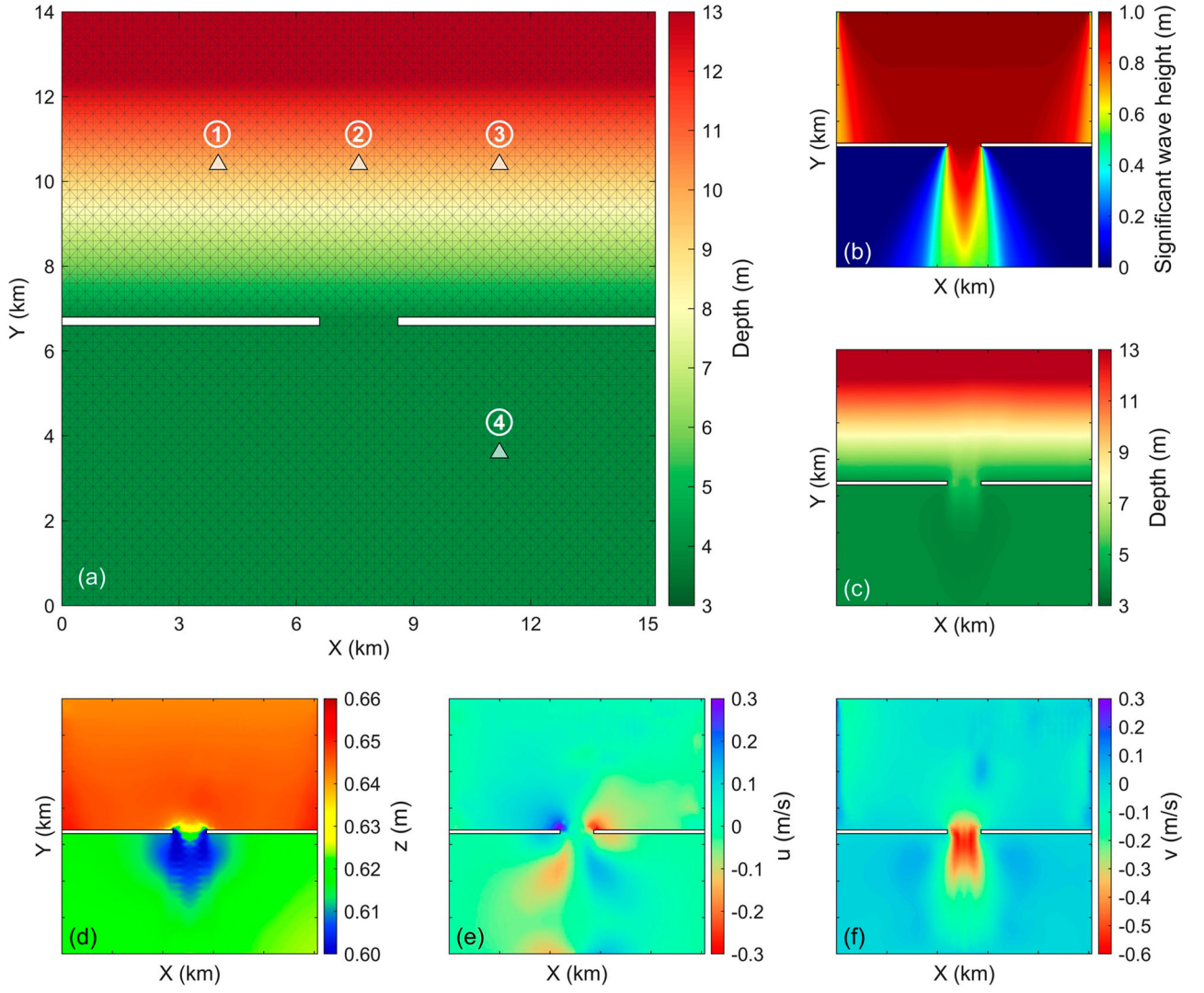

Figure 3. (a) Geometry, bathymetry, and mesh grid of the idealized tidal inlet case; (b) significant wave height incorporated in the FVCOM model; (c) example of morphological change during the simulation period. An example snapshot of the dataset is presented, including (d) water level, (e) eastward, and (f) northward components of current velocity in the bottom layer. White triangles in panel (a) represent four sites selected for time-series validation.

and output matrices share the same resolution: 1,000 m by 400 m in the (x, y) directions for the salinity case (E-1) and 400 m for the SSC case (T-1). Additionally, an enhanced-resolution scenario (T-5) is evaluated for SSC prediction, in which the input hydrodynamic data are at an 800 m resolution (low), and the output SSC data have a resolution of 200 m (high). To demonstrate this enhanced-resolution capability clearly, a comparison scenario (T4) is included, in which the 800 m resolution SSC data are directly interpolated to a 200 m high-resolution distribution. In all these scenarios, the focus is on the numerically simulated results of the bottom layer of the water column, as both saltwater intrusion and sediment movement are highly active near the bed. Besides, an additional scenario (T-6) targeting the surface layer is also included to investigate whether the substances in the surface layer can be equally well resolved as the bottom layer. The surface SSC may in the future also be extracted from satellite images, extending the practical future potential of our model.

The primary results (Sections 3.1 to 3.5) are presented based on idealized cases (E-1, T-1, T-2, T-3, T-5, and T-6), as these cases allow for more flexible dataset constructions than real-world scenarios. Additionally, a realistic case (N-1) is included to demonstrate the engineering application prospects of the proposed methodology. Case N-1 reflects actual hydrodynamic processes influenced by engineering structures constructed in the North Passage of the Changjiang Estuary. In 2016, we conducted comprehensive near-bed observations in the North

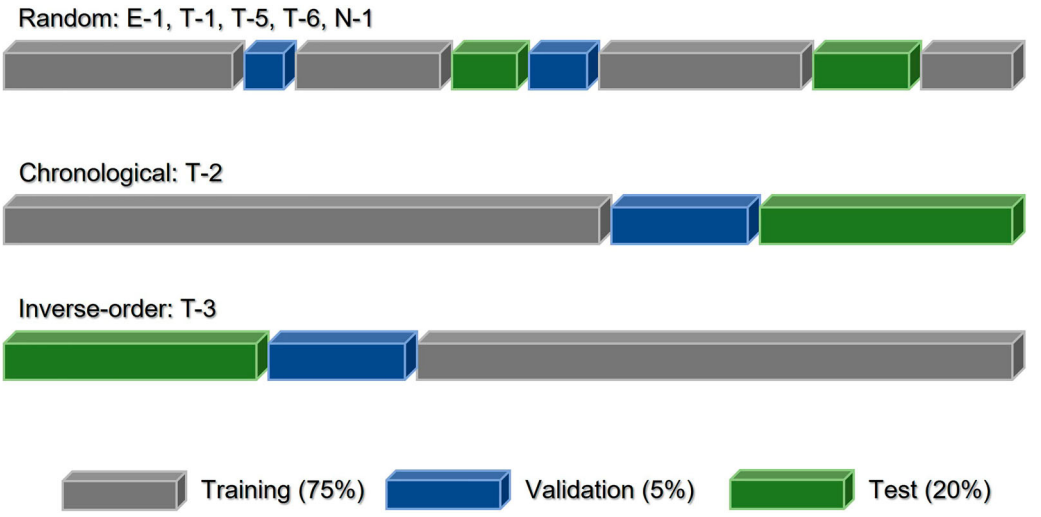

Figure 4. Diagram illustrating the random, chronological, and inverse-order sampling strategies for scenarios listed in Table 2, except for T-4, which is an interpolation scenario.

Passage and established a validated numerical model to help understand the estuarine system (Zhou et al., 2019). This numerical model provided a 5-day dataset of hydrodynamics and salinity variations with a temporal resolution of 15 minutes, which was subsequently used to train the DL model. The data sampling strategy for this case follows the standard scenarios (E-1 and T-1). Detailed results for Case N-1 will be presented in Section 3.6.

3. Results and discussion

We first present the results of loss functions (Figure 5) to illustrate the training process. The training losses gradually decrease with a converging pattern. Notably, the validation losses also exhibit an ideal decreasing tendency with a trend of gradual flattening, indicating that the model's architecture and training strategy effectively control overfitting. Although in Case E-1 the loss function still shows significant potential for further optimization (see blue lines in Figure 5), the accuracy is adequate for salinity prediction (as discussed in the following section). Therefore, the number of training epochs for all idealized scenarios is set to 50,000 for consistency. However, Case N-1, being a realistic scenario involving more complex geometry, bathymetry, and engineering impacts, requires a larger number of epochs; thus, the number of training epochs for this case is set to 100,000.

3.1. Salinity prediction: the engineered channel case

A comprehensive comparison between predicted salinity distribution and the ground truth data (Figure 6) demonstrates the feasibility of mapping hydrodynamics to salinity using our DL model. Results in Figure 6a–l are derived from 4 periods in the test set, corresponding to samples No. 440 (Figure 6a–c, $t = 13.111$ days), 455 (Figure 6d–f, $t = 13.215$ days), 471 (Figure 6g–I, $t = 13.326$ days), 505 (Figure 6j–l, $t = 13.563$ days) in the 1,000-sample salinity dataset. Note that the numerical model outputs data from $t = 10$ days onwards.

Due to spring-neap tidal dynamics and the effects of hydraulic engineering structures, salinity exhibits various spatiotemporal distributions with significant variations in both longitudinal and lateral directions. For instance, isolated salinity patches occur frequently around the heads of groynes (black boxes in Figure 6d–g). Such elaborate salinity structures pose challenges in accurately capturing the mapping relationship for the DL model. The residuals between ground truth data (i.e. data from numerical simulations) and the predicted salinity directly affirm the high accuracy of the DL model (Figure 6c,f,i, and l), as these residuals are almost invisible even with a color scale one order of magnitude smaller than the standard.

The RMSE and R^2 metrics are used to quantify the accuracy of the DL model (Figure 6m–o). These metrics are calculated based on all scattered values covering the entire spatiotemporal variations and are individually presented according to the training, validation, and test sets. Additionally, the relative errors are indicated by the color of these scattered points. The RMSE values on three partitioned sets are below 0.18, with the RMSE for the test set being very close to that for the validation set. The R^2 values are all above 0.999. Relative errors are well controlled, remaining under 10%, except for some smaller scattered values where the baseline values are very small.

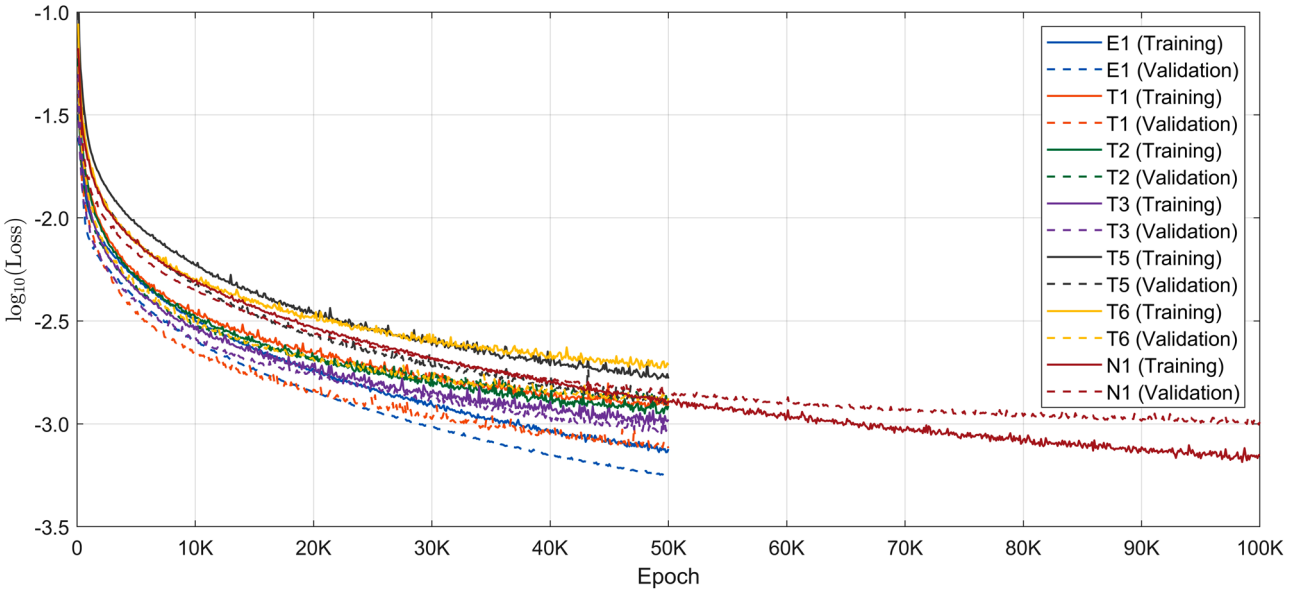

Figure 5. Logarithmic training and validation losses of all deep learning scenarios. See Table 2 for details on scenarios.

3.2. SSC prediction: the tidal inlet case

For the tidal inlet case, the DL model effectively captures the mapping relationship between hydrodynamics and SSC, even with the inclusion of more dynamic factors such as waves, winds, and topographic changes. Results for four temporal instances in the test set are shown in Figure 7, corresponding to No. 836, 845, 863, and 867 (t = 44.792, 45.167, 45.917, and 46.083 days, recording from t = 10 days) samples in the 1441-sample SSC dataset. At different stages within tidal cycles, the SSC distribution shows significant pattern variations, with high-SSC patches migrating up and down the inlet, shaped like an ellipse (Figure 7b) or triangle (Figure 7c). Due to the constant southwesterly wind, the SSC patches extend northeast during ebb tides. These characteristics are accurately learned and predicted by the DL model, as described below.

The residuals between the ground truth data (Figure 7a–d) and predicted SSC (Figure 7e–h) are well controlled, with visible differences occurring only at edges of SSC patches where horizontal gradients of SSC are most pronounced (Figure 7i–l). Despite these deviations, the DL model shows high accuracy in predicting the SSC. It should be noted that the SSC predicted and presented here is from the bottom layer of the water column, where the concentration is typically highest. In this study, the maximum SSC in the bottom layer is approximately 10 g/L, consistent with extremely high SSC detected in estuaries with turbidity maxima, for instance, the Changjiang Estuary (Zhu et al., 2022), the Loire Estuary (Dijkstra & de Goede, 2024), and the Yongjiang Estuary (Tao & Zhu, 2022). Furthermore, since the SSC dataset exhibits non-uniform distribution with higher SSC more concentrated in the first 20% of the recording period due to non-linear trends in addition to periodical variations, Cases T-2 and T-3 are designed to evaluate the effects on the representativeness of training data and the consequent model performance.

Table 3. The maximum and average SSC of training, validation, and test sets in Cases T-1, T-2, and T-3, respectively.

	Maximum SSC			Average SSC		
	Training	Validation	Test	Training	Validation	Test
T-1	11.267	10.627	11.296	1.032	1.033	1.036
T-2	11.296	7.418	9.158	1.046	0.850	1.031
T-3	10.004	8.394	11.296	1.011	0.934	1.139

The temporally non-uniform distribution of SSC is indicated by the maximum and average values of each dataset (Table 3). Random sampling (Case T-1) shows a close range of SSC values in the partitioned datasets, as particularly indicated by the average SSC. This approach is a common sampling strategy applied in deep learning. In contrast, for the chronological (T-2) and inverse-order (T-3) sampling strategies, the relative magnitudes of maximum and average SSC in the training and the test sets are exactly opposite.

As a result, random sampling leads to similar performance across each set (Figure 8a–c). The RMSE values are kept below 0.0450 g/L and the R^2 values are greater than 0.999. In Case T-2, the DL model achieves comparable performance on the training and validation sets compared to Case T-1 (Figure 8d and e). The RMSE of the test set is about 0.01 g/L higher than that of T-1 (Figure 8f), which is still satisfactory for SSC prediction.

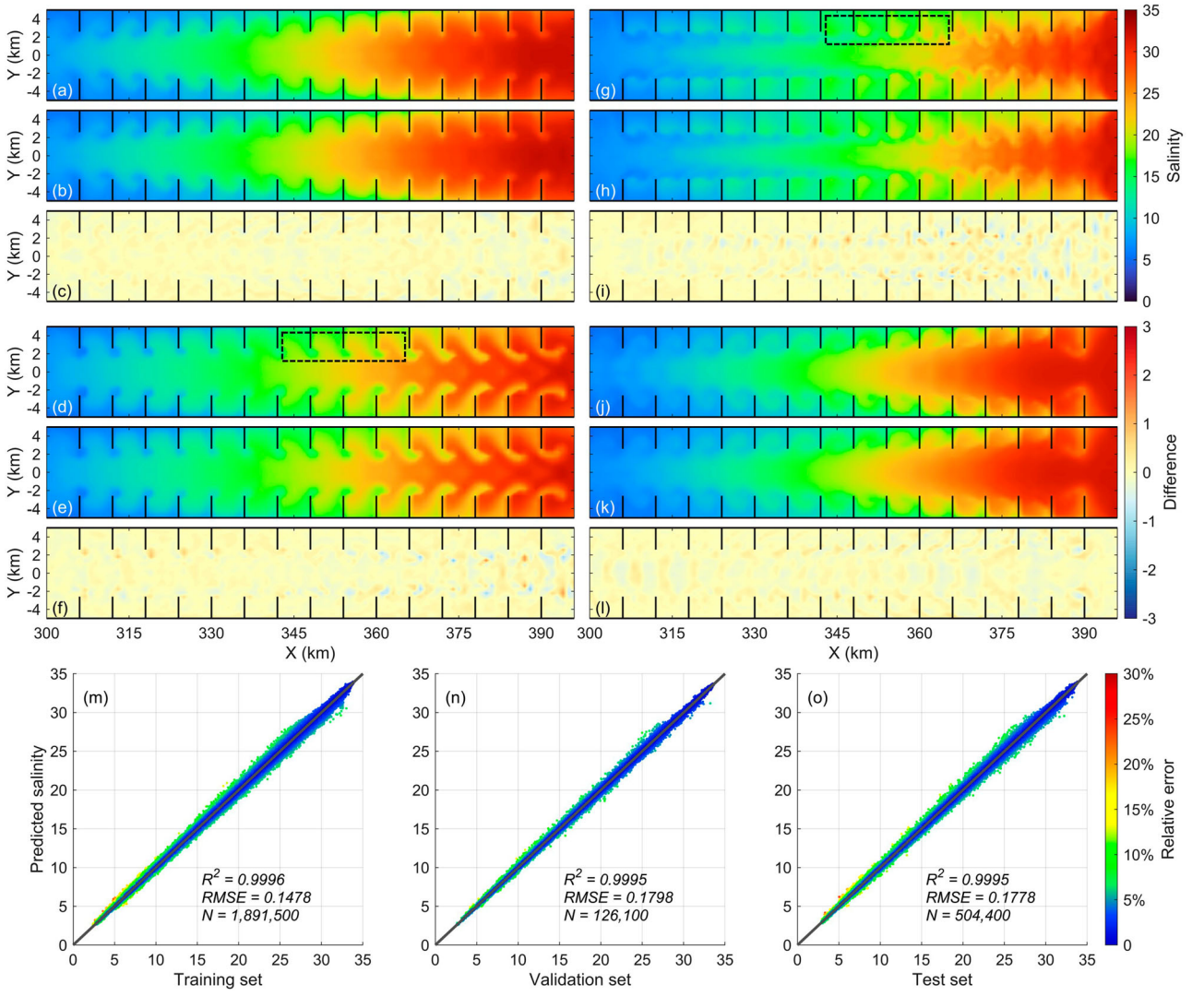

Figure 6. Salinity distribution at four temporal instances of Case E-1 and overall evaluations. Panels (a, d, g, j) display the ground truth data, while panels (b, e, h, k) show the salinity predictions provided by the DL model. All these temporal instances belong to the test set. Panels (c, i, f, l) are differences between panels (a, g, d, j) and (b, h, e, k), respectively. The RMSE and R^2 values for all scattered points, covering the entire spatiotemporal variation of salinity, are presented in panels (m, n, o) for the training, validation, and test sets, respectively. Black boxes in panels (d, g) highlight salinity patches around the heads of groynes.

Furthermore, the RMSEs of the training and validation sets in Case T-3 (Figure 8g and h) are even higher than those in Cases T-1 and T-2. However, the RMSE of the test set increases to approximately 3.4 times that of the standard scenario (Figure 8i).

The relative errors in Figure 8i show that the DL model performs relatively well in extrapolating to high SSC (> 10 g/L), which is beyond the range of the training set (Figure 8g). This indicates the capability of the DL model for extrapolation to extreme values. The errors are more pronounced for SSC < 6 g/L, which falls within the range of the training data. These results suggest that for this specific SSC dataset, different mapping relationships (rather than just the magnitude of SSC) exist in different parts of the dataset due to data distribution skewness. In other words, it is crucial for the sampling method to sufficiently ensure representativeness in the training set. Therefore, the random sampling method applied in the standard scenario T-1 is recommended as the primary choice.

3.3. Enhanced-Resolution prediction

The potential of the model to predict relatively high-resolution substance distribution based on low-resol ution hydrodynamics can further improve the value and applicability of the framework proposed in this study. Therefore, Case T-5 is designed to evaluate its performance in terms of enhancing resolution. In Case T-5, the high-resolution (200 m) outputs of the numerical model are processed differently: the hydrodynamics (z, u, v) are

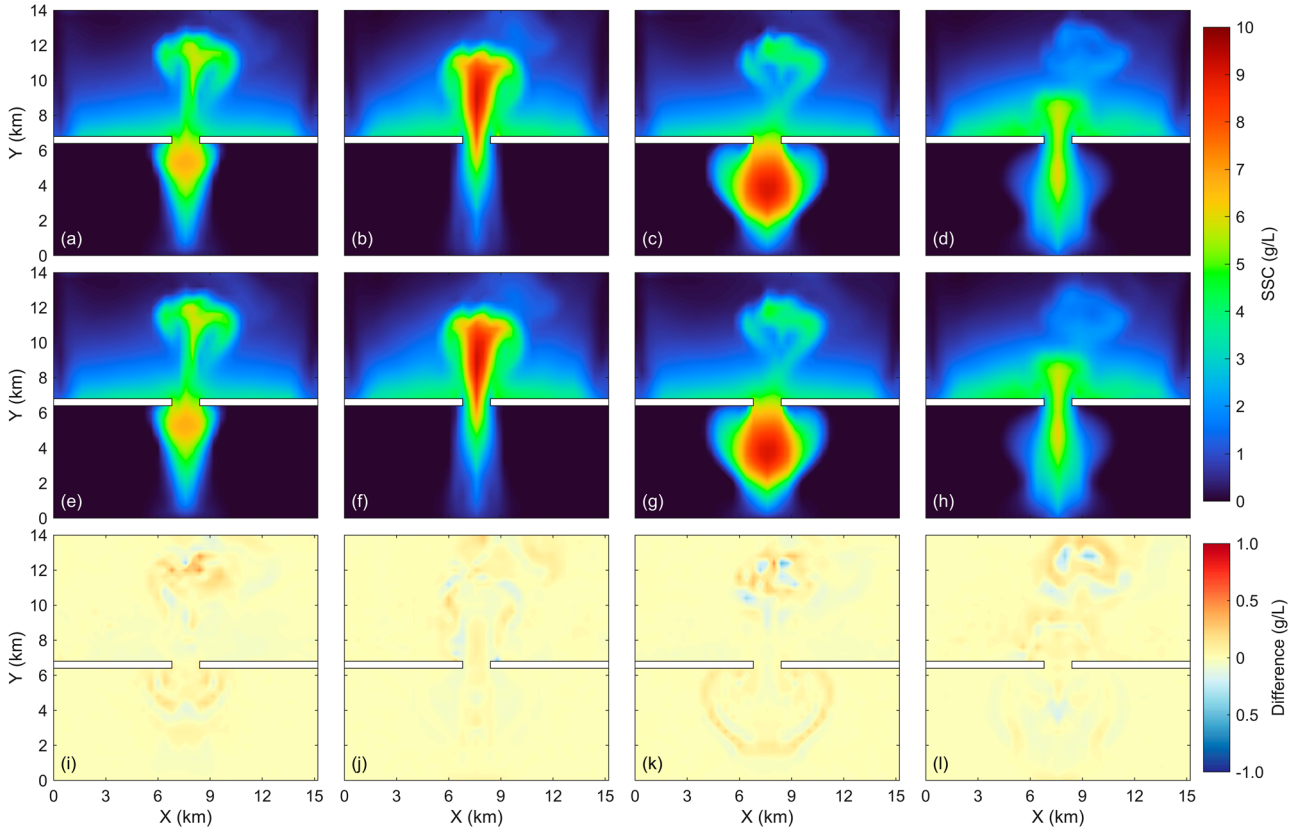

Figure 7. Distribution of suspended sediment concentration (SSC) at four temporal instances of Case T-1. Panels (a, b, c, d) display ground truth data, while panels (e, f, g, h) show the SSC predictions provided by the DL model. These temporal instances are all part of the test set. Panels (i, j, k, l) illustrate the differences between panels (a, b, c, d) and panels (e, f, g, h), respectively. Each column represents a temporal instance in the test set.

interpolated into a low-resolution (800 m) grid, while the target (SSC) retains the high resolution (200 m), creating a 1:16 difference in resolution between the inputs and outputs of the DL model. Note that the high resolution of target substance distribution is still needed in the training set, but when applying the well-trained DL model for prediction, only low-resolution input of hydrodynamics is required.

The drawbacks of low resolution are presented in Figure 9a. Geometrically, the width of barrier islands is distortedly enlarged, and information at the open boundary is missing due to low-resolution resampling from the numerical model output. More importantly, the SSC distribution loses detailed and smooth characteristics compared to the high-resolution data (Figure 9c). Although a direct interpolation using natural neighbor method can help complete the missing data in the domain (Figure 9b), the SSC distribution significantly differs from the high-resolution data. Two main differences should be noted (marked by two white boxes in Figure 9b): first, the high-SSC patch in the open sea lacks detailed anchor-shape features; and second, the SSC at the narrow inlet is much lower than in the high-resolution data.

Enhanced-resolution prediction can solve the problem of information missing and accuracy declining (Figure 9d). The errors associated with interpolation and enhanced-resolution prediction are visualized in Figure 9e and f, respectively. The errors from interpolation (Figure 9e) are much higher than those from enhanced-resolution prediction (Figure 9f), with large errors corresponding to both the domain boundaries and the shapes of SSC patches. Statistically, the RMSE of the test set in enhanced-resolution prediction is only 5.66% of the RMSE in the interpolation case, demonstrating the accuracy of the DL model in enhanced-resolution prediction. Consequently, the framework introduced in this study can be further developed and applied to resolve high-resolution substance distribution using only low-resolution, fast, and computationally economic numerical models or other data sources which cannot provide the high resolution.

3.4. Time-series validation

Previous sections have thoroughly demonstrated how the framework is constructed and applied, as well as its

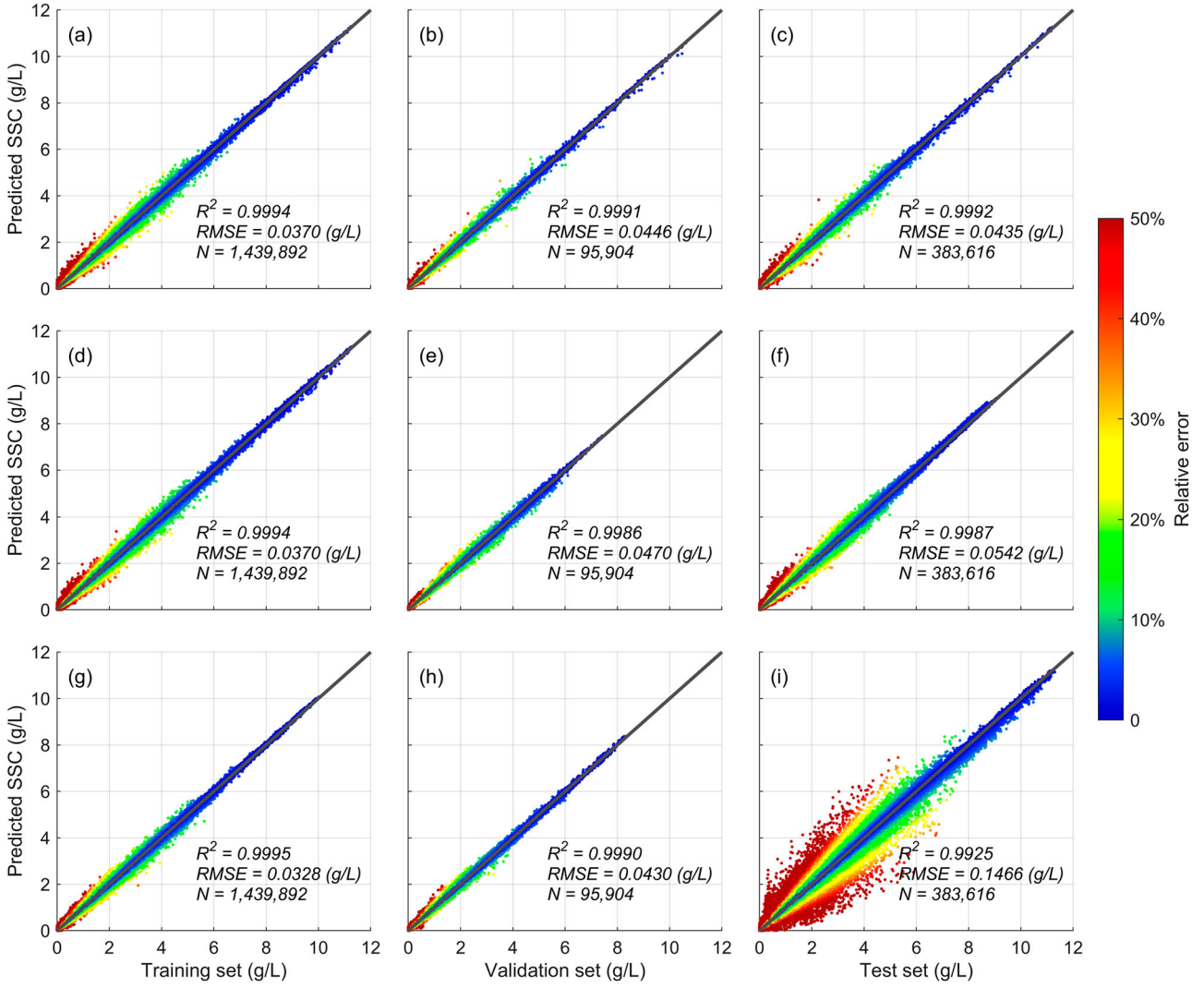

Figure 8. The RMSE and R^2 values of all scattered points, covering the entire spatiotemporal variation of SSC, are presented for training (first column), validation (second column), and test (third column) sets, respectively. Three data partitioning strategies are employed, including random (Case T-1, first row), chronological (Case T-2, second row), and inverse-order (T-3, third row) sampling methods.

capability in predicting substance distribution. Nevertheless, the framework also shows valuable potential for broader application scenarios. In this and the following sections, two extended scenarios are discussed to further evaluate the DL model.

While the spatial distribution clearly illustrates the transport process of the substance of interest, in lots of circumstances, time-series variations are also crucial. Time-series information directly reflects the evolutionary trends of specific variables at important sites and is more convenient for comparison with thresholds for catastrophic events. For instance, continuous observations of salinity at Qingcaosha, Baozhen, and Sheshan stations are important indicators (Zhu et al., 2020) of saltwater intrusion, which may severely hinder the freshwater supply for the Changjiang River Delta Economic Zone. Therefore, the accuracy of time-series prediction is also essential for broader applications.

In Case E-1, the DL model provides accurate salinity predictions at the 4 sites marked in Figure 2c. The RMSEs calculated at these sites based on the test set are well controlled below 0.2 (Figure 10), which constitutes only about 1% of the average salinity at these sites in the test set. For Case T-1, a similar time-series validation was conducted at the 4 sites denoted in Figure 3a. The RMSEs are relatively higher than those of salinity prediction due to more complex dynamics considered in numerical simulations. The RMSEs and their proportion relative to the average SSC in the test set reveal that among the 4 sites, prediction errors are more notable at Sites 2 and 3 in Figure 3a, where the SSC fluctuates the most (Figure 11).

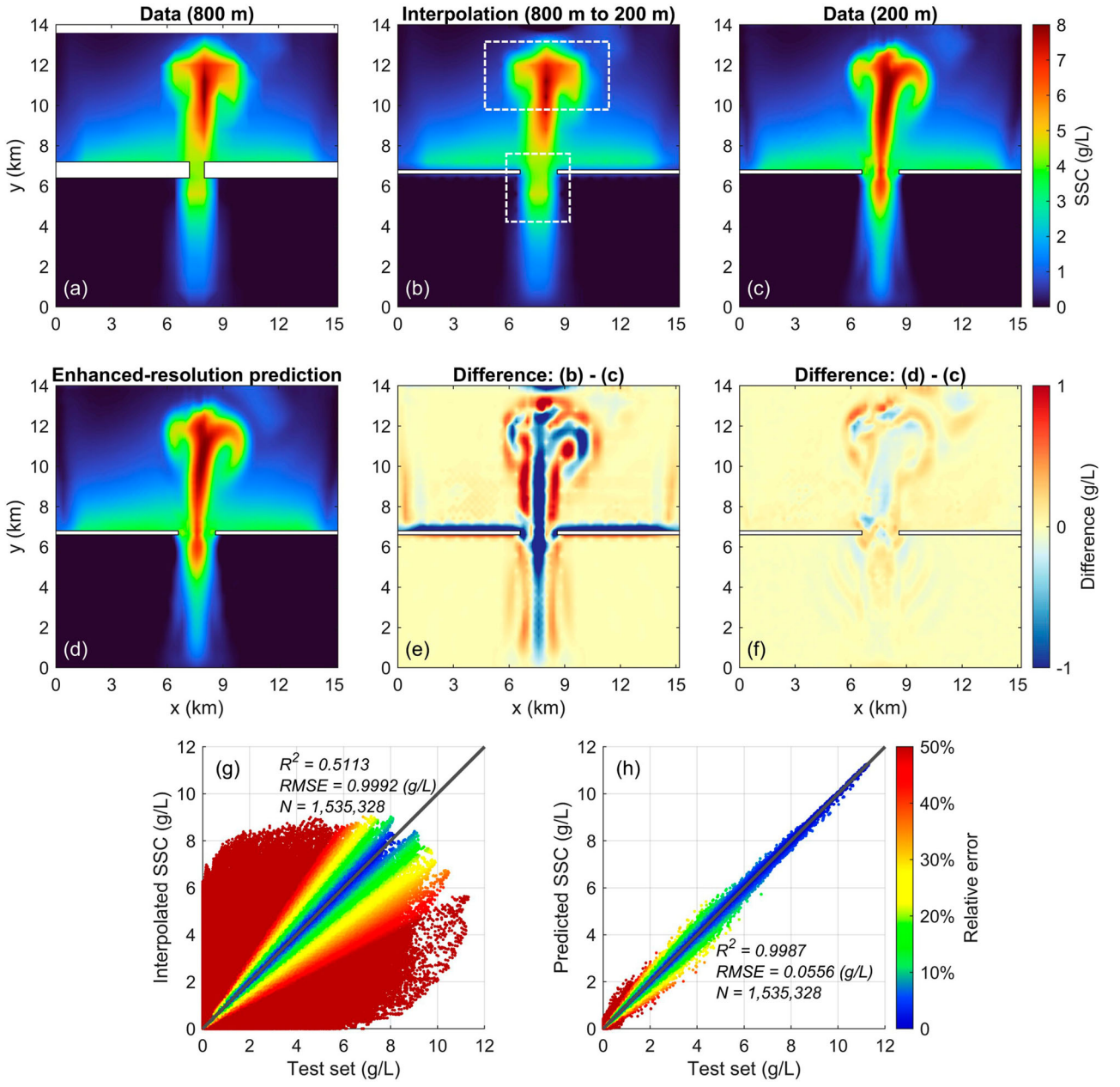

Figure 9. Low-resolution (800 m) data derived from the numerical model (a); a direct natural neighbor interpolation from the low-resolution data to a high-resolution (200 m) grid (b), i.e. Case T-4; high-resolution data derived from the numerical model (c); the enhanced-resolution prediction by the DL model which takes low-resolution hydrodynamics as input then outputs the high-resolution SSC (d), i.e. Case T-5; panels (e) and (f) show the differences between panels (b) and (c), (d) and (c), respectively. The RMSE and R^2 values of all scattered points, covering the whole spatiotemporal variation of SSC in the test set, are presented for direct interpolation (g) and enhanced-resolution prediction (h). The white dashed boxes indicate the accuracy issue induced by interpolation.

Nevertheless, these results still verify the model performance for SSC prediction, as the highest ratio of RMSE to the average is only 4.23% (Figure 11c). Therefore, the accuracy of the DL model is further demonstrated by this time-series validation, indicating that this framework can be effectively applied in time-series prediction at individual stations.

3.5. Surface layer prediction

Another important consideration is that all the variables (except for water levels) mentioned earlier in this study are extracted from the bottom layer of the water column due to the following reasons. For salinity, saltwater intrusion would be firstly detected in the bottom layer due to gravitational effects; therefore, accurate prediction for

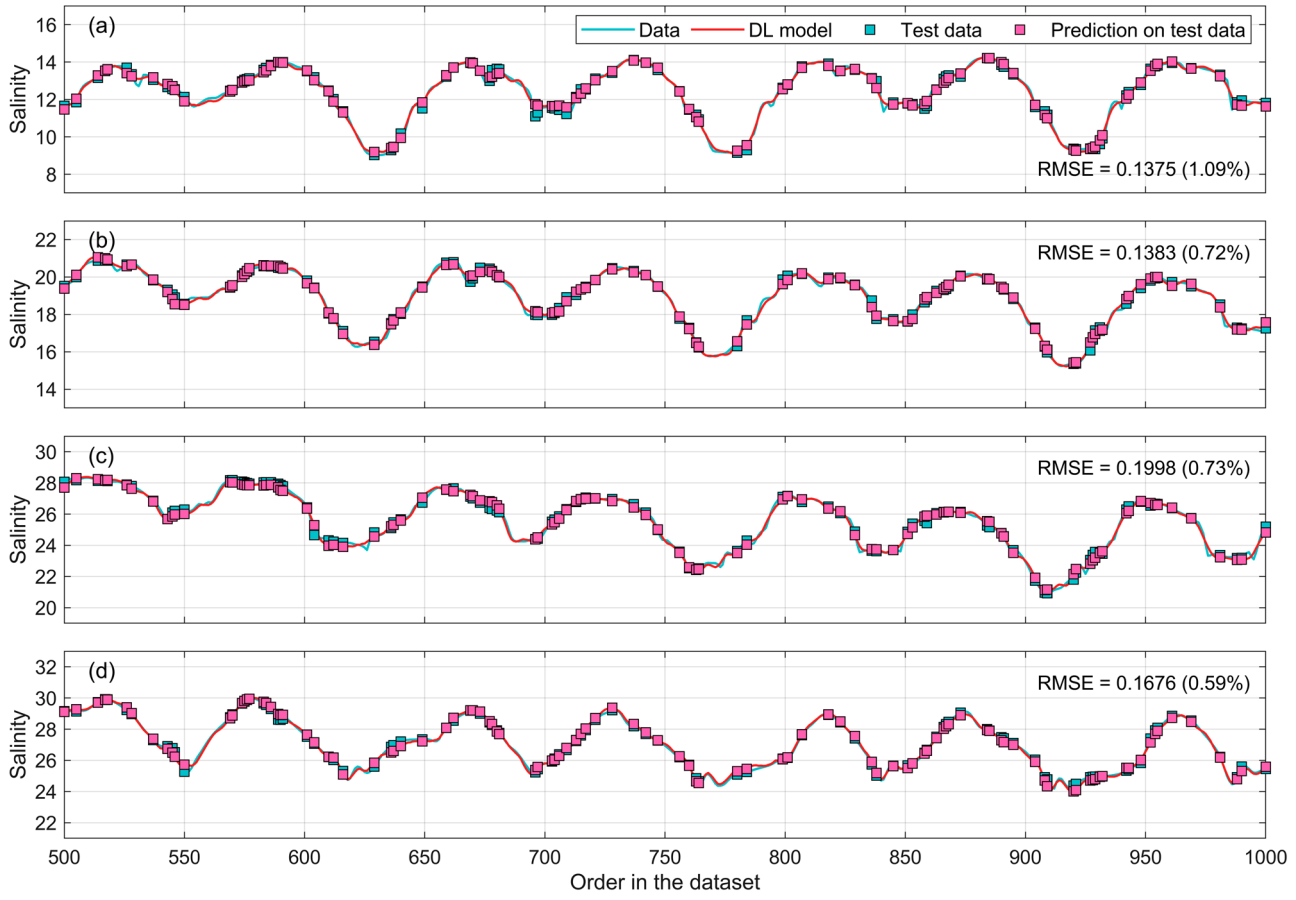

Figure 10. Time-series validation for salinity prediction at four sites. Panels (a-d) correspond to the numbered sites in Figure 2c. The percentage values in brackets are the ratios of RMSE values to the average salinity at these sites in the test set.

bottom salinity is of practical importance. For SCC, the bottom SSC is crucial for morphological changes and typically exhibits a wider range of fluctuations, which aids in examining the model capability of predicting extremely high SSC and visualizing spatiotemporal variations in SSC.

However, since sediment is initialized from the sea bed by shear stress, the mapping relationship between hydrodynamics and sediment near the bed is expected to be more prominent and easier to capture. Whether a strong mapping relationship still exists in other layers of the water column, under the influence of complex processes such as advection and settling, requires further investigation. On the other hand, due to advancements in remote sensing techniques (Dethier et al., 2020; Volpe et al., 2011), the turbidity of the surface layer has become potential data source for SSC that can be observed on a large spatial scale at a high resolution and provided as model training data. Consequently, examining the performance of the DL model using the surface layer SSC data is beneficial for extending our framework for future practical applications.

The results of Case T-6 demonstrate the robust performance of the DL model. The maximum of RMSEs for the three partitioned sets are only 0.025 g/L, and the R^2 values exceed 0.990. The high accuracy of SSC prediction for the surface layer indicates a strong mapping relationship between hydrodynamics and SSC at the surface, moreover, which our DL model successfully captures. However, it should be noted that this mapping relationship is relatively weaker compared to that in the bottom layer. This is firstly indicated by the recorded training process (Figure 5), as the remaining training and validation losses (yellow lines) after 50,000 epochs are higher than in other cases. Secondly, it is also supported by the statistic information, as RMSEs in Figure 12m–o (surface layer prediction) are greater than those in Figure 8a–c (bottom layer prediction). This aligns with our understanding of sediment dynamics. The good performance of the method in the surface layer suggests its potential for integration with additional data sources, such as satellite images and high frequency ground-wave radar systems, which can monitor large-scale water levels and surface currents (Martin et al., 2022; Paduan & Washburn, 2013; Wang et al., 2021)

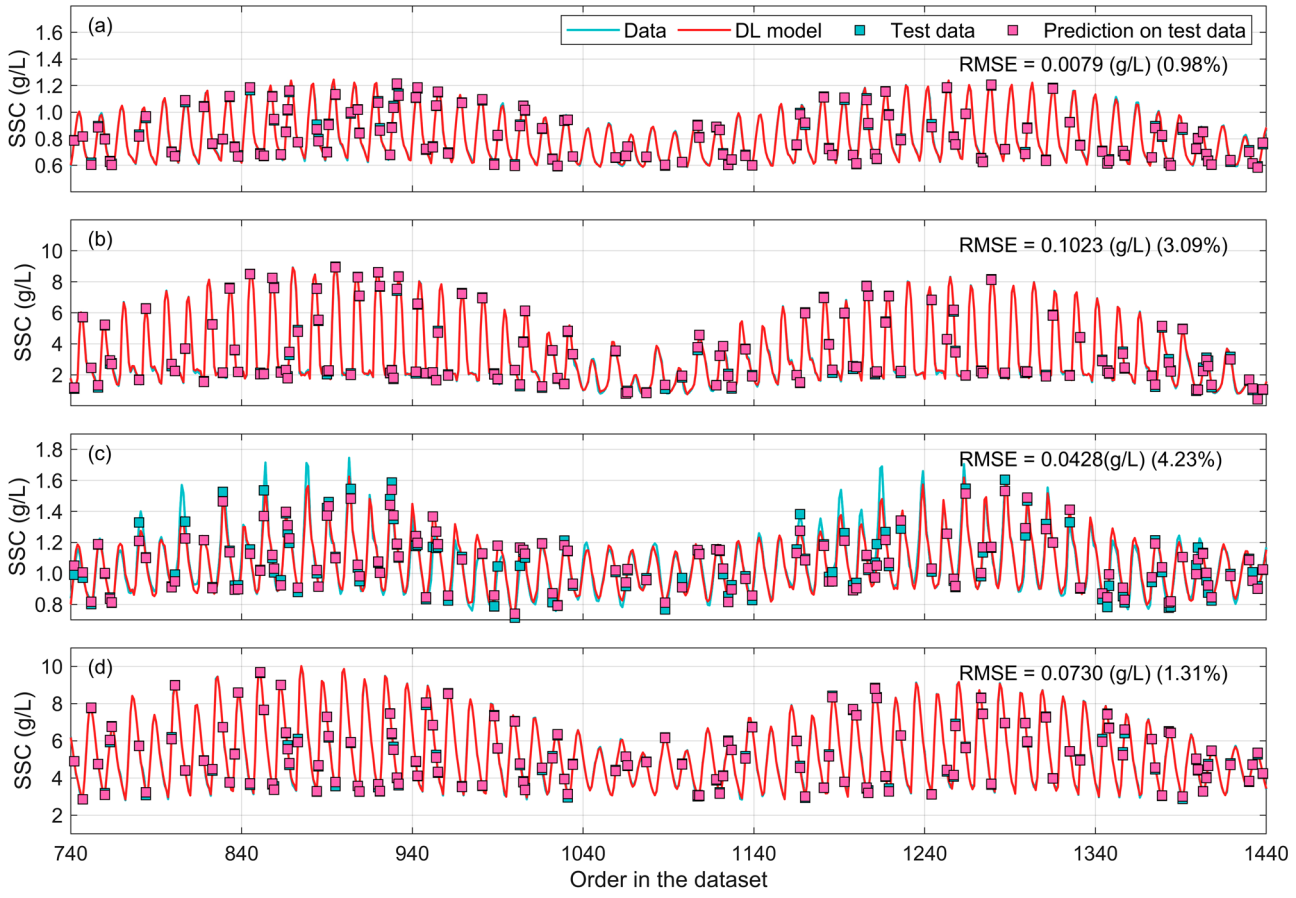

Figure 11. Time-series validation for salinity prediction at four sites. Panels (a-d) correspond to the numbered sites in Figure 3a. The percentage values in brackets are the ratios of RMSE values to the average SSC at these sites in the test set.

as inputs for our framework to predict spatiotemporal substance distribution.

3.6. Real-world application

The proposed framework was further applied to the North Passage (NP) of the Changjiang Estuary to evaluate its efficacy in a real-world scenario. The NP is characterized by the Deep Navigation Channel Project, which includes two long dikes and multiple perpendicular groynes (Figure 13a). These rigid engineering structures regulate the flow field by enhancing mainstream current velocities. Meanwhile, salinity variations in this region have been extensively documented in previous studies (e.g. Li et al., 2020; Wu et al., 2010), being driven by longitudinal advection but also cross-section lateral density flows (Zhou et al., 2019). These complex dynamics make the NP an ideal system for validating whether the proposed framework can effectively capture the relationship between a complex flow field and salinity distribution under the influence of realistic engineering structures.

In 2016, comprehensive in-situ observations were conducted using a tripod frame to monitor near-bed hydrodynamics and salinity variations. The observational site is indicated by a pentagram in Figure 13d. Detailed descriptions of the measurements and the published dataset can be found in Z. Zhou et al. (2025a). Subsequently, an FVCOM model was established and validated to hindcast the dynamics processes (Zhou et al., 2019), providing the dataset utilized in this study. The salinity distribution predicted by the DL model shows an R^2 value of 0.9982 and RMSE of 0.2980 (Figure 13b). Although these error levels are slightly higher compared to the idealized engineered-channel scenario (E–1), the performance of the DL model remains highly acceptable. The robustness of the DL model is further validated by time-series comparisons at the observational site, accurately reproducing numerical model results and closely capturing observed patterns (Figure 13c). Visualization of the predicted salinity fields (Figure 13d–l) demonstrates that the detailed spatial patterns can be effectively captured by the DL model, including phenomena such as saltwater trapping in groyne fields (Figure 13g–h). The NP case not only confirms the robustness of the DL

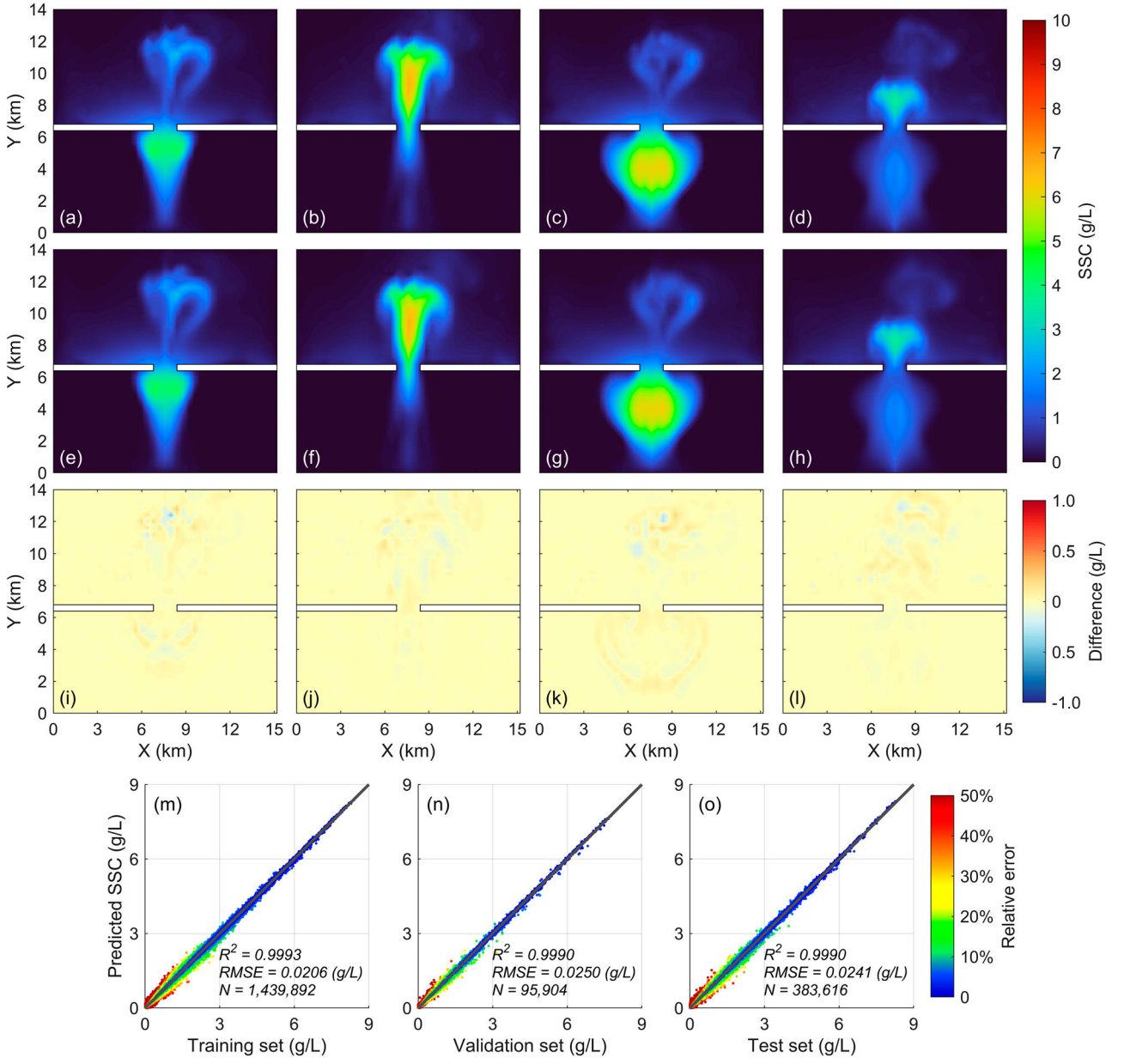

Figure 12. Distribution of SSC of the surface layer in the water column at four temporal instances of Case T-6. Panels (a, b, c, d) display the ground truth data; panels (e, f, g, h) show predicted SSC provided by the DL model. These temporal instances are the same with those in Figure 7. Panels (i, j, k, l) are differences between panels (a, b, c, d) and (e, f, g, h), respectively. The RMSE and R^2 values of all scattered points, covering the whole spatiotemporal variation of SSC, are presented for training (m), validation (n), and test (o) sets.

model but also validates the feasibility of predicting SIFs solely based on hydrodynamic conditions in realistic scenarios. It thus provided additional technical options for water quality forecasting and related disaster prediction applications.

3.7. Challenges and future work

The framework and the included DL model show great potential across various application scenarios. Using a data-driven method to infer the distribution of SIFs based on basic hydrodynamics has proven feasible. However, several challenges remain with the current methodology, limiting its extensive application in real-world complex scenarios. The method emphasizes the spatiotemporal distribution of substances, requiring training data that adequately represent both temporal and spatial dimensions, thereby imposing a higher data requirement. Due to the difficulty in fulfilling the large data demands of such data-driven models, many studies have incorporated physical laws (governing equations) into deep learning models, such as the physics-informed neural

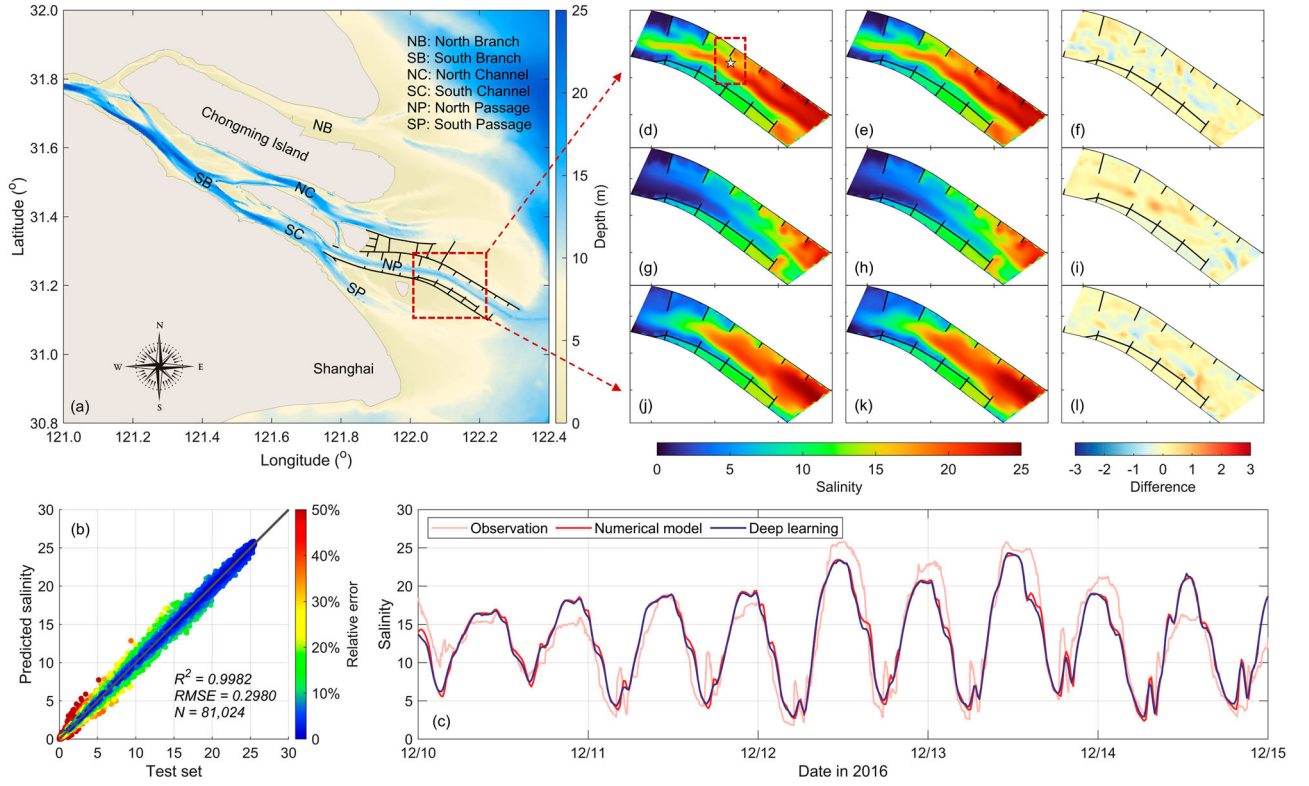

Figure 13. (a) Bathymetry of the Changjiang Estuary and adjacent regions. Dikes and groynes constructed in the North Passage are indicated by black lines. (b) The RMSE and R^2 values of all scattered points, covering the entire spatiotemporal variation of salinity, for the test set in Case N-1. (c) Time-series comparison of near-bed salinity among in-situ observations (blue), numerical model results (red), and DL model predictions (pink). The observational site is marked by the pentagram in panel (d). Panels (d – l) illustrate the salinity distribution at four temporal instances from the test set; columns represent the ground truth data (first column), DL predictions (second column), and their differences (third column), respectively.

networks (PINNs) (Raissi et al., 2019; Zhou et al., 2025b) and physics-informed neural operators (PINOs) (Li et al., 2024). These methods successfully alleviate the issue of data requirement but also complicate model training due to challenges such as unbalanced terms in loss functions (Rohrhofer et al., 2022; Wang et al., 2022). Nevertheless, integrating physical equations with data-driven models remains promising, especially when high-quality marine data are difficult to obtain. This inspires consideration of incorporating physics into the framework in the future.

The realizations shown in this study utilize data generated by numerical simulations. Although employing numerical models to generate datasets is a commonly adopted strategy (Huang et al., 2022; Li & Shatarah, 2024), reliance on numerical results inevitably limits the applicability and efficiency of the proposed framework, especially during the inferring stage, as (1) numerical simulations become a prerequisite in this case and (2) the quality of these numerical simulations may become a limiting factor (especially if high-quality data can be an alternative – see below). On the one hand, the enhanced-resolution capability of the DL model partially alleviates this limitation by reducing the computational cost required to prepare numerical results as input data. On the other hand, a promising alternative approach is to integrate other data sources, such as satellite-based products and image-based hydrometry techniques, to serve as both inputs and outputs of the DL model during training process. Once the mapping relationships have been established by the DL model based on existing available datasets, incomplete data can also potentially be supplemented. For instance, remote sensing data gaps caused by adverse weather conditions could be filled through further developments of our framework. SSC in complex estuarine environments is difficult to predict, even with well-calibrated numerical models. When additional data sources, such as satellite-based surface SSC observations, are incorporated into the training dataset, the DL model may bypass errors inherent in numerical simulations by directly learning mapping relationships from observational data. As indicated by Cases T-1, T-2, and T-3, improving representativeness and coverage within the training datasets significantly influences the model's extrapolation capability. Thus, it is recommended to fully

leverage existing data products with longer temporal coverage to include extreme values as many as possible in future studies.

In this study, salinity and SSC are examined as examples. They exhibit distinct properties, resulting in differing mechanisms of transport and distribution in aquatic environments. The proposed methodology demonstrates robust predictive capability for the distribution of both substances, thereby validating the reliability of the model. Our future work aims to include a broader variety of substances, such as temperature, dissolved oxygen, and algae, addressing concerns related to physics, chemistry, and biology in water research. Furthermore, for substances that are featured with active processes, such as algae that grow and perish, we will investigate the feasibility of predicting their concentration and distribution based on hydrodynamic characteristics. If the model's performance proves inadequate, we will consider incorporating additional key influencing factors to improve the model's efficacy.

4. Conclusions

We developed a framework to predict the spatiotemporal distribution of substances in fluids based on water levels and flow velocities. The framework includes a deep learning model which applies the architecture of a classic neural operator, DeepONet. The deep learning model incorporates a feature network and a position network, which are used to encode the features of input variables and problem geometry, respectively. Different from the original DeepONet, a convolutional neural network is applied in the feature network to extract spatiotemporal information from the input variables and enable resolution-enhanced inference. Numerical simulations were conducted to provide training data for the deep learning model.

The framework was tested by predicting the salinity and SSC distribution derived from two idealized cases and one real-world case. The accuracy of predictions with different data sampling methods proves not only the robustness of the deep learning model but also the importance of representativeness of the training set. The model was also demonstrated to be able to enhance the resolution of predictions, enabling more computationally economic predictions as low-resolution hydrodynamics can be utilized to construct a high-resolution substance distribution. Both the bottom and surface layers of the water column were examined using the framework. We found that the mapping relationship from hydrodynamics to substance distribution can be captured throughout the entire water column although exhibiting different intensity, broadening the application scope of the framework. It shows potential for further integration with additional data sources other than numerical simulations in the future, such as remote sensing data, which primarily targets the water surface.

Highlights

(1) A deep learning framework is developed to predict spatiotemporal distribution of substances in fluids based on basic hydrodynamic data.
(2) Salinity and suspended sediment concentration are accurately predicted by the proposed framework.
(3) The deep learning model can provide substance output at a higher spatial resolution than hydrodynamic input.

Author contributions

CRediT: **Zaiyang Zhou:** Conceptualization, Formal analysis, Methodology, Software, Writing – original draft; **Yu Kuai:** Data curation, Visualization, Writing – review & editing; **Kailin Huang:** Formal analysis, Methodology; **Dirk Sebastiaan van Maren:** Methodology, Writing – review & editing; **Jialin Pang:** Software, Validation; **Zhenwu Wang:** Methodology, Software; **Yonghui Zhu:** Formal analysis, Visualization; **Jianzhong Ge:** Conceptualization, Writing – review & editing

Disclosure statement

No potential conflict of interest was reported by the author(s).

Funding

This research is supported by the National Natural Science Foundation of China [grant number 42406161, 42476160, and 41776104], the National Key Research and Development Program of China [grant number 2022YFE0117500], and the Key Research Program of Shanghai Municipal Oceanic Bureau (Key Technology Research and Application of Marine Intelligent Grid Forecasting for Shanghai [grant number HHK-2023-06]).

Data availability statement

Data are publicly available at https://figshare.com/s/b02d6c61e02e47275ed4.

References

Amoudry, L. O., & Souza, A. J. (2011). Deterministic coastal morphological and sediment transport modeling: A review and discussion. *Reviews of Geophysics*, *49*(2), 1–21. https://doi.org/10.1029/2010RG000341

Beardsley, R. C., Chen, C., & Xu, Q. (2013). Coastal flooding in scituate (MA): A FVCOM study of the 27 December 2010 nor'easter. *Journal of Geophysical Research: Oceans*, *118*(11), 6030–6045. https://doi.org/10.1002/2013JC008862

Bi, K., Xie, L., Zhang, H., Chen, X., Gu, X., & Tian, Q. (2023). Accurate medium-range global weather forecasting with 3D neural networks. *Nature*, *619*(7970), 533–538. https://doi.org/10.1038/s41586-023-06185-3

Bosboom, J., & Reniers, A. J. H. M. (2014). Displacement-based error metrics for morphodynamic models. *Advances in Geosciences*, *39*, 37–43. https://doi.org/10.5194/adgeo-39-37-2014

Chen, C., Huang, H., Beardsley, R. C., Liu, H., Xu, Q., & Cowles, G. (2007). A finite volume numerical approach for coastal ocean circulation studies: Comparisons with finite difference models. *Journal of Geophysical Research: Oceans*, *112*, C03018. https://doi.org/10.1029/2006JC003485

Chen, C., Malanotte-Rizzoli, P., Wei, J., Beardsley, R. C., Lai, Z., Xue, P., Lyu, S., Xu, Q., Qi, J., & Cowles, G. W. (2009). Application and comparison of Kalman filters for coastal ocean problems: An experiment with FVCOM. *Journal of Geophysical Research: Oceans*, *114*, 1–17. https://doi.org/10.1029/2007JC004548

Chen, T., & Chen, H. (1995). Universal approximation to nonlinear operators by neural networks with arbitrary activation functions and its application to dynamical systems. *IEEE Transactions on Neural Networks*, *6*(4), 911–917. https://doi.org/10.1109/72.392253

Cugier, P., & Le Hir, P. (2002). Development of a 3D hydrodynamic model for coastal ecosystem modelling. Application to the Plume of the Seine River (France). *Estuarine, Coastal and Shelf Science*, *55*(5), 673–695. https://doi.org/10.1006/ecss.2001.0875

de Swart, H. E., & Zimmerman, J. T. F. (2009). Morphodynamics of tidal inlet systems. *Annual Review of Fluid Mechanics*, *41*(1), 203–229. https://doi.org/10.1146/annurev.fluid.010908.165159

Dethier, E. N., Renshaw, C. E., & Magilligan, F. J. (2020). Toward improved accuracy of remote sensing approaches for quantifying suspended sediment: Implications for suspended-sediment monitoring. *Journal of Geophysical Research: Earth Surface*, *125*(7). https://doi.org/10.1029/2019JF005033

Dijkstra, Y. M., & de Goede, R. J. A. (2024). Regime shift to hyperturbid conditions in the Loire estuary: Overview of observations and model analysis of physical mechanisms. *Journal of Geophysical Research: Oceans*, *129*(9), e2023JC020273. https://doi.org/10.1029/2023JC020273

Eltner, A., Elias, M., Sardemann, H., & Spieler, D. (2018). Automatic image-based water stage measurement for long-term observations in ungauged catchments. *Water Resources Research*, *54*(12), 10,362–10,371. https://doi.org/10.1029/2018WR023913

Feizizadeh, B., Garajeh, M. K., Lakes, T., & Blaschke, T. (2021). A deep learning convolutional neural network algorithm for detecting saline flow sources and mapping the environmental impacts of the Urmia lake drought in Iran. *CATENA*, *207*, 105585. https://doi.org/10.1016/j.catena.2021.105585

Garcia, P. D., Matheus, D. M., & Gireli, T. Z. (2024). Sedimentation analysis of the maritime stretch after dredging activities for widening and deepening Santos' Port Channel. *Ocean & Coastal Management*, *258*, 107383. https://doi.org/10.1016/j.ocecoaman.2024.107383

Ge, J., Lu, J., Zhang, J., Chen, C., Liu, A., & Ding, P. (2022). Saltwater intrusion-induced flow reversal in the changjiang estuary. *Journal of Geophysical Research: Oceans*, *127*, 1–19. https://doi.org/10.1029/2021JC018270

Ge, J., Torres, R., Chen, C., Liu, J., Xu, Y., Bellerby, R., Shen, F., Bruggeman, J., & Ding, P. (2020). Influence of suspended sediment front on nutrients and phytoplankton dynamics off the Changjiang Estuary: A FVCOM-ERSEM coupled model experiment. *Journal of Marine Systems*, *204*, 103292. https://doi.org/10.1016/j.jmarsys.2019.103292

Gilmore, T. E., Birgand, F., & Chapman, K. W. (2013). Source and magnitude of error in an inexpensive image-based water level measurement system. *Journal of Hydrology*, *496*, 178–186. https://doi.org/10.1016/j.jhydrol.2013.05.011

Goldstein, E. B., Coco, G., & Plant, N. G. (2019). A review of machine learning applications to coastal sediment transport and morphodynamics. *Earth-Science Reviews*, *194*, 97–108. https://doi.org/10.1016/j.earscirev.2019.04.022

Guo, W., Wang, X. H., Ding, P., Ge, J., & Song, D. (2018). A system shift in tidal choking due to the construction of Yangshan Harbour, Shanghai, China. *Estuarine, Coastal and Shelf Science*, *206*, 49–60. https://doi.org/10.1016/j.ecss.2017.03.017

He, J., Kushwaha, S., Park, J., Koric, S., Abueidda, D., & Jasiuk, I. (2024). Sequential Deep Operator Networks (S-DeepONet) for predicting full-field solutions under time-dependent loads. *Engineering Applications of Artificial Intelligence*, *127*, 107258. https://doi.org/10.1016/j.engappai.2023.107258

Huang, S., Xia, J., Wang, Y., Wang, W., Zeng, S., She, D., & Wang, G. (2022). Coupling machine learning into hydrodynamic models to improve river modeling with complex boundary conditions. *Water Resources Research*, *58*, 1–15. https://doi.org/10.1029/2022WR032183

Huang, Y., Chen, H., Huang, K., Chen, M., Wang, J., & Liu, B. (2024). Optimization of space-time image velocimetry based on deep residual learning. *Measurement*, *232*, 114688. https://doi.org/10.1016/j.measurement.2024.114688

Huettel, M., Berg, P., & Kostka, J. E. (2014). Benthic exchange and biogeochemical cycling in permeable sediments. *Annual Review of Marine Science*, *6*(1), 23–51. https://doi.org/10.1146/annurev-marine-051413-012706

Hunter, J. M., Maier, H. R., Gibbs, M. S., Foale, E. R., Grosvenor, N. A., Harders, N. P., & Kikuchi-Miller, T. C. (2018). Framework for developing hybrid process-driven, artificial neural network and regression models for salinity prediction in river systems. *Hydrology and Earth System Sciences*, *22*(5), 2987–3006. https://doi.org/10.5194/hess-22-2987-2018

Lam, R., Sanchez-Gonzalez, A., Willson, M., Wirnsberger, P., Fortunato, M., Alet, F., Ravuri, S., Ewalds, T., Eaton-Rosen, Z., Hu, W., Merose, A., Hoyer, S., Holland, G., Vinyals, O., Stott, J., Pritzel, A., Mohamed, S., & Battaglia, P. (2023). Learning skillful medium-range global weather forecasting. *Science*, *382*(6677), 1416–1421. https://doi.org/10.1126/science.adi2336

Lesser, G. R., Roelvink, J. A., van Kester, J. A. T. M., & Stelling, G. S. (2004). Development and validation of a three-dimensional morphological model. *Coastal Engineering*, *51*(8-9), 883–915. https://doi.org/10.1016/j.coastaleng.2004.07.014

Li, H., & Shatarah, M. (2024). Operator learning for urban water clarification hydrodynamics and particulate matter transport with physics-informed neural networks. *Water Research*, *251*, 121123. https://doi.org/10.1016/j.watres.2024.121123

Li, L., Zhu, J., Chant, R. J., Wang, C., & Pareja-Roman, L. F. (2020). Effect of dikes on saltwater intrusion under various wind conditions in the Changjiang estuary. *Journal of Geophysical Research: Oceans*, *125*, 1–25. https://doi.org/10.1029/2019JC015685

Li, Z., Zheng, H., Kovachki, N., Jin, D., Chen, H., Liu, B., Azizzadenesheli, K., & Anandkumar, A. (2024). Physics-informed neural operator for learning partial differential equations. *ACM / IMS Journal of Data Science*, *1*(3), 1–27. https://doi.org/10.1145/3648506

Lu, L., Jin, P., Pang, G., Zhang, Z., & Karniadakis, G. E. (2021). Learning nonlinear operators via DeepONet based on the universal approximation theorem of operators. *Nature Machine Intelligence*, *3*(3), 218–229. https://doi.org/10.1038/s42256-021-00302-5

Luo, J., Straffelini, E., Bozzolan, M., Zheng, Z., & Tarolli, P. (2023). Saltwater intrusion in the Po River Delta (Italy) during drought conditions: Analyzing its Spatio-temporal evolution and potential impact on agriculture. *International Soil and Water Conservation Research*, *12*(3), 714–725. https://doi.org/10.1016/j.iswcr.2023.09.009

Martin, A. C. H., Gommenginger, C. P., Jacob, B., & Staneva, J. (2022). First multi-year assessment of Sentinel-1 radial velocity products using HF radar currents in a coastal environment. *Remote Sensing of Environment*, *268*, 112758. https://doi.org/10.1016/j.rse.2021.112758

Mei, Y., Zhang, Y., Zhu, X., Gou, R., & Gao, J. (2024). Fully convolutional network-enhanced DeepONet-based surrogate of predicting the travel-time fields. *IEEE Transactions on Geoscience and Remote Sensing*, *62*, 1–12. https://doi.org/10.1109/TGRS.2024.3401196

Miranda, L. S., Wijesiri, B., Ayoko, G. A., Egodawatta, P., & Goonetilleke, A. (2021). Water-sediment interactions and mobility of heavy metals in aquatic environments. *Water Research*, *202*, 117386. https://doi.org/10.1016/j.watres.2021.117386

Mondal, P., Walter, M., Miller, J., Epanchin-Niell, R., Gedan, K., Yawatkar, V., Nguyen, E., & Tully, K. L. (2023). The spread and cost of saltwater intrusion in the US Mid-Atlantic. *Nature Sustainability*, *6*(11), 1352–1362. https://doi.org/10.1038/s41893-023-01186-6

Morales-Marin, L. A., French, J. R., Burningham, H., & Battarbee, R. W. (2018). Three-dimensional hydrodynamic and sediment transport modeling to test the sediment focusing hypothesis in upland lakes. *Limnology and Oceanography*, *63*, S156–S176. https://doi.org/10.1002/lno.10729

Olabarrieta, M., Geyer, W. R., & Kumar, N. (2014). The role of morphology and wave-current interaction at tidal inlets: An idealized modeling analysis. *Journal of Geophysical Research: Oceans*, *119*(12), 8818–8837. https://doi.org/10.1002/2014JC010191

Paduan, J. D., & Washburn, L. (2013). High-frequency radar observations of ocean surface currents. *Annual Review of Marine Science*, *5*(1), 115–136. https://doi.org/10.1146/annurev-marine-121211-172315

Papanicolaou, A. (T.) N., Elhakeem, M., Krallis, G., Prakash, S., & Edinger, J. (2008). Sediment transport modeling review—current and future developments. *Journal of Hydraulic Engineering*, *134*(1), 1–14. https://doi.org/10.1061/(ASCE)0733-9429(2008)134:1(1)

Pathak, J., Subramanian, S., Harrington, P., Raja, S., Chattopadhyay, A., Mardani, M., Kurth, T., Hall, D., Li, Z., Azizzadenesheli, K., Hassanzadeh, P., Kashinath, K., & Anandkumar, A. (2022). FourCastNet: A global data-driven high-resolution weather model using adaptive Fourier Neural operators.

Raissi, M., Perdikaris, P., & Karniadakis, G. E. (2019). Physics-informed neural networks: A deep learning framework for solving forward and inverse problems involving nonlinear partial differential equations. *Journal of Computational Physics*, *378*, 686–707. https://doi.org/10.1016/j.jcp.2018.10.045

Ridderinkhof, W., de Swart, H. E., van der Vegt, M., Alebregtse, N. C., & Hoekstra, P. (2014). Geometry of tidal inlet systems: A key factor for the net sediment transport in tidal inlets. *Journal of Geophysical Research: Oceans*, *119*(10), 6988–7006. https://doi.org/10.1002/2014JC010226

Roelvink, J. A. (2006). Coastal morphodynamic evolution techniques. *Coastal Engineering*, *53*(2-3), 277–287. https://doi.org/10.1016/j.coastaleng.2005.10.015

Rohrhofer, F. M., Posch, S., Gößnitzer, C., & Geiger, B. C. (2022). *On the role of fixed points of dynamical systems in training physics-informed neural networks*, 1–22.

Shi, S., Xu, Y., Li, W., & Ge, J. (2022). Long-term response of an estuarine ecosystem to drastic nutrients changes in the Changjiang River during the last 59 years: A modeling perspective. *Frontiers in Marine Science*, *9*, 1–21. https://doi.org/10.3389/fmars.2022.1012127

Song, T., Wang, Z., Xie, P., Han, N., Jiang, J., & Xu, D. (2020). A novel dual path gated recurrent unit model for sea surface salinity prediction. *Journal of Atmospheric and Oceanic Technology*, *37*(2), 317–325. https://doi.org/10.1175/JTECH-D-19-0168.1

Stoecker, D. K., Hansen, P. J., Caron, D. A., & Mitra, A. (2017). Mixotrophy in the marine plankton. *Annual Review of Marine Science*, *9*(1), 311–335. https://doi.org/10.1146/annurev-marine-010816-060617

Tao, J., & Zhu, R. (2022). Exploring the three-dimensional flow-sediment dynamics and trapping mechanisms in a curved estuary: The role of salinity and circulation. *Frontiers in Marine Science*, *9*, 1–21. https://doi.org/10.3389/fmars.2022.976332

Volpe, V., Silvestri, S., & Marani, M. (2011). Remote sensing retrieval of suspended sediment concentration in shallow waters. *Remote Sensing of Environment*, *115*(1), 44–54. https://doi.org/10.1016/j.rse.2010.07.013

Wang, N., & Ge, J. (2025). Predictions of saltwater intrusion in the changjiang estuary: Integrating machine learning methods with FVCOM. *Journal of Hydrology*, *653*, 132739. https://doi.org/10.1016/j.jhydrol.2025.132739

Wang, P., Bayram, B., & Sertel, E. (2022). A comprehensive review on deep learning based remote sensing image super-resolution methods. *Earth-Science Reviews*, *232*, 104110. https://doi.org/10.1016/j.earscirev.2022.104110

Wang, S., Yu, X., & Perdikaris, P. (2022). When and why PINNs fail to train: A neural tangent kernel perspective. *Journal of Computational Physics*, *449*, 110768. https://doi.org/10.1016/j.jcp.2021.110768

Wang, X., He, X., Xiao, R., Song, M., & Jia, D. (2021). Millimeter to centimeter scale precision water-level monitoring using

GNSS reflectometry: Application to the South-to-North Water Diversion Project, China. *Remote Sensing of Environment*, *265*, 112645. https://doi.org/10.1016/j.rse.2021.112645

Winterwerp, J. C., Van Kessel, T., Van Maren, B., & Van Prooijen, B. C. (2021). Fine sediment in open water: From fundamentals to modeling, advanced series on ocean engineering. *World Scientific*, 550 pp.

Wu, H., Zhu, J., & Ho Choi, B. (2010). Links between saltwater intrusion and subtidal circulation in the Changjiang Estuary: A model-guided study. *Continental Shelf Research*, *30*(17), 1891–1905. https://doi.org/10.1016/j.csr.2010.09.001

Wu, L., Chen, C., Guo, P., Shi, M., Qi, J., & Ge, J. (2011). A FVCOM-based unstructured grid wave, current, sediment transport model, I. Model description and validation. *Journal of Ocean University of China*, *10*(1), 1–8. https://doi.org/10.1007/s11802-011-1788-3

Xie, D., Hughes, Z., FitzGerald, D., Tas, S., Asik, T. Z., & Fagherazzi, S. (2024). Longshore sediment transport across a tombolo determined by two adjacent circulation cells. *Journal of Geophysical Research: Earth Surface*, *129*, 1–23. https://doi.org/10.1029/2024JF007709

Xue, P., Chen, C., Ding, P., Beardsley, R. C., Lin, H., Ge, J., & Kong, Y. (2009). Saltwater intrusion into the Changjiang River: A model-guided mechanism study. *Journal of Geophysical Research: Oceans*, *114*, 1–15. https://doi.org/10.1029/2008JC004831

Zhang, R., Xiong, W., Ma, X., & Cai, C. S. (2024). Mesh-free SPH modelling of sediment scouring and flushing considering grains transport and transformation. *Engineering Applications of Computational Fluid Mechanics*, *18*(1), 2367510. https://doi.org/10.1080/19942060.2024.2367510

Zhang, S., Wu, J., Wang, Y.-G., Jeng, D.-S., & Li, G. (2022). A physics-informed statistical learning framework for forecasting local suspended sediment concentrations in marine environment. *Water Research*, *218*, 118518. https://doi.org/10.1016/j.watres.2022.118518

Zhou, J., Sun, B., Zhang, H., Yuan, S., & Tang, H. (2025). Numerical investigation of nonlinear interaction between salinity- and sediment-induced stratification in highly turbid estuaries and coastal seas. *Engineering Applications of Computational Fluid Mechanics*, *19*(1), 2443123. https://doi.org/10.1080/19942060.2024.2443123

Zhou, Z., Ge, J., van Maren, D. S., Kuai, Y., Ding, P., & Wang, Z. B. (2024). Groyne-induced effects on channel-shoal exchange and saltwater intrusion in estuarine environments. *Journal of Hydraulic Engineering*, *150*(1), 1–15. https://doi.org/10.1061/JHEND8.HYENG-13500

Zhou, Z., Ge, J., van Maren, D. S., Luan, H., Guo, W., Ma, J., Tao, Y., Xu, P., Dao, F., Yang, W., Ke, K., Shi, S., Zhang, J., Kuai, Y., Li, C., Gu, J., & Ding, P. (2025a). Multi-year observations of near-bed hydrodynamics and suspended sediment at the core of the estuarine turbidity maximum of the Changjiang Estuary. *Earth System Science Data*, *17*, 917–935. https://doi.org/10.5194/essd-17-917-2025

Zhou, Z., Ge, J., van Maren, D. S., Wang, Z. B., Kuai, Y., & Ding, P. (2021). Study of sediment transport in a tidal channel-shoal system: Lateral effects and slack-water dynamics. *Journal of Geophysical Research: Oceans*, *126*(3), e2020JC016334. https://doi.org/10.1029/2020JC016334

Zhou, Z., Ge, J., Wang, Z. B., Maren, D. S., Ma, J., & Ding, P. (2019). Study of lateral flow in a stratified tidal channel-shoal system: The importance of intratidal salinity variation. *Journal of Geophysical Research: Oceans*, *124*(9), 6702–6719. https://doi.org/10.1029/2019JC015307

Zhou, Z., Kuai, Y., Ge, J., van Maren, B., Wang, Z., Huang, K., Ding, P., & Wang, Z. (2025b). Modeling non-stationary wind-induced fluid motions with physics-informed neural networks for the shallow water equations in a polar coordinate system. *Water Resources Research*, *61*(1), e2024WR037490. https://doi.org/10.1029/2024WR037490

Zhu, C., van Maren, D. S., Guo, L., Lin, J., He, Q., & Wang, Z. B. (2022). Feedback effects of sediment suspensions on transport mechanisms in an estuarine turbidity maximum. *Journal of Geophysical Research: Oceans*, *127*, 1–15. https://doi.org/10.1029/2021JC018029

Zhu, J., Cheng, X., Li, L., Wu, H., Gu, J., & Lyu, H. (2020). Dynamic mechanism of an extremely severe saltwater intrusion in the changjiang estuary in February 2014. *Hydrology and Earth System Sciences*, *24*(10), 5043–5056. https://doi.org/10.5194/hess-24-5043-2020